https://doi.org/10.5194/egusphere-2025-3202
Preprint. Discussion started: 14 October 2025

Implementation of predicted rime mass in the bin microphysics scheme DESCAM 3D: Heavy Snowfall event during ICE-POP 2018

Pierre Grzegorczyk[1], Wolfram Wobrock[1], Antoine Canzi[1], Frédéric Tridon[2,1], Gyuwon Lee[3], Kwonil Kim[4], Kyo-Sun Sunny Lim[3], and Céline Planche[1,5]

[1]Université Clermont Auvergne, CNRS INSU, Laboratoire de Météorologie Physique UMR 6016, F-63000 Clermont-Ferrand, France
[2]DIATI, Politecnico di Torino, Turin, Italy
[3]BK21 Weather Extremes Education and Research Team, Department of Atmospheric Sciences, Center for Atmospheric REmote sensing (CARE), Kyungpook National University, Daegu, Republic of Korea
[4]School of Marine and Atmospheric Sciences, Stony Brook University, Stony Brook, New York, USA
[5]Institut Universitaire de France (IUF), Paris, France

Correspondence: Pierre Grzegorczyk (p.grzegorczyk@opgc.fr) and Céline Planche (celine.planche@uca.fr)

Abstract. Due to their wide variety of properties, the representation of ice particles in cold and mixed-phase clouds are challenging to represent for microphysical schemes. To improve their representation, this study evaluates the implementation of predicted rime mass distribution in the bin microphysics scheme DESCAM. Based on the ‘fill-in’ concept, the model allows a smooth transition in ice particle properties between unrimed and graupel particles. Consequently, the terminal velocity and collision kernels of ice particles were updated as a function of rime fraction. These implementations are tested for a heavy snowfall event observed from March 7–9 during the ICE-POP 2018 field campaign in the mountainous Pyeongchang region of the Korean Peninsula. This event consists of a deep cloud triggered by a low-pressure system, followed by a shallower cloud system formed by orographic lifting of marine air. We found that the rime mass fraction at ground simulated by DESCAM evolves similarly to the rime index measured by the MASC instrument. Furthermore, during the shallow cloud phase, the predicted rime implementation leads to an increase in ice particle number concentration and a decrease in mean particle size (from 1.5 to 1.0 mm). The new version of DESCAM leads to significant changes in the spatial distribution of precipitation, with strong local variations exceeding 10 mm, resulting in an increase of 6.5% in total precipitation amount. Accounting for predicted rime mass gives a better agreement between the model and the ground based observations of ICE-POP 2018.

1 Introduction

The formation of precipitating ice particles results from a complex combination of microphysical processes including vapor deposition, aggregation, and riming. Consequently, ice particles exhibit a wide variety of shapes (Kikuchi et al., 2013) depending on environmental conditions.

In mixed-phase clouds, riming occurs when precipitating ice particles collect supercooled liquid droplets down to -25°C (Tridon et al., 2022). As riming depletes supercooled liquid water, it significantly impacts the phase partitioning of mixed-phase clouds, which plays an important role on the Earth’s radiation budget (Matus and L’Ecuyer, 2017; Korolev et al., 2017).

Riming of ice particles has been widely documented from various observations, including radars (Mason et al., 2018; Kneifel and Moisseev, 2020), in-situ aircraft (Waitz et al., 2022; Maherndl et al., 2024) or even ground based measurements (Praz et al., 2017). During riming, small droplet tends to 'fill-in' the empty spaces within the structure of ice particles, increasing their density (Heymsfield, 1982; Seifert et al., 2019). Therefore, rimed ice crystals (i.e. graupel or hail) have a fastest terminal velocity (Vázquez-Martín et al., 2021) which explains their key role on precipitation. Indeed, several observational studies demonstrate the significant influence of riming on precipitation such as Grazioli et al. (2015) who showed its impact on precipitation flux, or Mitchell et al. (1990) who found that 30 to 40% of snow was formed by rime in Sierra Nevada. Similarly, Moisseev et al. (2017) reported that riming accounted for 5% to 40% of snowfall in a frontal system in Finland. Furthermore, riming also plays an important role for secondary ice production (SIP) mechanisms (Korolev and Leisner, 2020) such as the Hallett-Mossop (rime splintering) process (Hallett and Mossop, 1974), fragmentation during thermal shock (King and Fletcher, 1976) or fragmentation due to graupel-graupel collisions (Takahashi et al., 1995; Grzegorczyk et al., 2023; Yadav et al., 2024).

A wide variety of modeling studies also reported the important role of riming of graupel particles on the precipitation evolution and amount (Morrison and Milbrandt, 2011; McMillen and Steenburgh, 2015; Poirier et al., 2019; Li et al., 2019; Jin et al., 2019). In models, the habit of ice crystals is often represented by distinct categories (e.g., ice, snow, graupel, or hail) in most bulk microphysics schemes (e.g., WRF: Thompson et al., 2008; Morrison et al., 2009; Lim and Hong, 2010; ICON: Seifert and Beheng, 2006; Meso-NH: Vié et al., 2016; Pinty and Jabouille, 1998) or even bin microphysics schemes (e.g., HUCM: Khain et al., 2004; UPNB: Geresdi, 1998; Geresdi et al., 2014). One of the major difficulty when categorizing ice crystals is to parameterize the transfer between the distinct ice categories (i.e., conversion or autoconversion rates), which is often set as a tuning parameter. In nature, ice particles have complex morphologies, necessitating a large number of categories and thus increase the number of uncertain conversion rates. Furthermore, as noted by Morrison and Grabowski (2008), categorizing ice particle types (e.g., ice and snow categories) is less straightforward than the distinction between cloud droplets and raindrops.

Instead of separating ice particles into categories, a new approach focuses on predicting their properties, allowing free evolution along their history. The first implementations following this approach were introduced by Hashino and Tripoli (2007); Morrison and Grabowski (2008, 2010) in both bulk and bin schemes. The approach of Morrison and Grabowski (2010) considers the 'filling in' of crystal interstices during riming as introduced by the observations of Heymsfield (1982). It assumes that rime fills the ice particle interstices, increasing its mass while keeping it the same size. The 'fill-in' continues until the interstices (such as the branches of dendrites or the faces of ice plates) are completely filled of rime. At this point, the ice crystal can be considered as a graupel for which additional rime increases both its mass and its size.

The ICE-POP 2018 campaign (International Collaborative Experiments for Pyeongchang 2018 Olympic and Paralympic Winter Games) took place during the 2018 winter Olympic Games over the mountainous region of Pyeongchang, located in the eastern part of the Korean peninsula. One of the main goal of this campaign was to investigate the ice particles properties of winter snowfall events using ground-based remote sensing instruments and microphysical probes (Jeoung et al., 2020; Gehring et al., 2020b; Kim et al., 2021; Gehring et al., 2021). Several snowfall events were investigated by Ko et al. (2022); Sunny Lim et al. (2020) in order to assess of the ability of the double moment 6-class (WDM6) scheme (Lim and Hong, 2010) to reliably predict the ice particles properties. Additionally, the ICE-POP 2018 observations were also used to evaluate the implementation

https://doi.org/10.5194/egusphere-2025-3202
Preprint. Discussion started: 14 October 2025

of prognostic graupel and snow number concentration (Kwon et al., 2023) as well as predicted graupel volume mixing ratio (Park et al., 2024) in WDM6 scheme.

This study aims to evaluate the implementation of a predicted rime mass distribution in the bin microphysics scheme DESCAM (DEtailed SCAvening and Microphysics model, Flossmann and Wobrock, 2010; Planche et al., 2010) based on the approach of Morrison and Grabowski (2010). Originally representing ice particles by a single predicted number distribution divided into 39 mass bins, the present implementation will allow to refine the ice particle behavior within each bin of DESCAM, including size, fall speed, and collision kernels, as a function of rime mass. The benefits of this implementation will be assessed by comparing the ice particle properties and precipitation outcomes predicted by DESCAM to a heavy snowfall event observed during ICE-POP 2018.

This paper is structured as follows: Section 2 describes the implementation of the predicted rime mass distribution in DESCAM model. Section 3 presents the case study, including the numerical setup and the instrumentation used during the ICE-POP 2018 campaign. Section 4 presents the results of DESCAM simulations and evaluates them against measurements from the ICE-POP 2018 campaign. Finally, Section 5 summarizes the main conclusions of the study.

2 Implementation of a rime distribution in DESCAM

2.1 DESCAM microphysics scheme

DESCAM (DEtailed SCAvening and Microphysics model, Flossmann and Wobrock, 2010; Planche et al., 2010) is a bin microphysics currently included in the 3D cloud scale model of Clark (Clark et al., 1996; Clark, 2003). It predicts five distribution functions, each divided in 39 mass bins with namely, interstitial aerosol particles, liquid drops, ice particles as well as aerosol mass inside drop and ice particles.

The aerosol particle distribution of DESCAM ranges from 1 nm to 6 μm diameter, while liquid drops ranges from 2 μm to 13 mm diameter. Aerosol activation follows Köhler theory (Leroy et al., 2007). Liquid drops evolve through condensation, evaporation, and deactivation, as well as collision-coalescence, collision-breakup, and dynamical breakup. Aerosol-cloud interactions and liquid phase processes of DESCAM have been investigated by numerous studies (Flossmann et al., 1985; Flossmann, 1998; Planche et al., 2010, 2013b; Flossmann and Wobrock, 2019; Arteaga et al., 2020; Kagkara et al., 2020).

The distribution of ice particles follows the same mass bins as for drops. The primary ice formation mechanisms, including heterogeneous and homogeneous ice nucleation, are implemented following Hiron and Flossmann (2015). Secondary ice production mechanisms including Hallett-Mossop process (Hallett and Mossop, 1974), fragmentation due to ice-ice collisions (Grzegorczyk et al., 2023; Yadav et al., 2024), and fragmentation of freezing drops (Phillips et al., 2018) were recently implemented by Grzegorczyk et al. (2025a). Ice particles are growing by vapor deposition, sublimation, riming and aggregation. Several studies performed with DESCAM model also focused on cold microphysics processes (Leroy et al., 2009; Planche et al., 2013a; Grzegorczyk et al., 2025b).

https://doi.org/10.5194/egusphere-2025-3202
Preprint. Discussion started: 14 October 2025

2.2 Ice particle size

In the original version of DESCAM (Flossmann and Wobrock, 2010), the size of the ice particles was fixed and calculated by the mass-diameter ($m-D$) relation:

$$m = \alpha D^{\beta} \tag{1}$$

with D and m the ice particle diameter (in cm) and mass (in g), α = 0.0038 and β = 2.08 are two coefficients obtained from the in situ aicraft observations of Fontaine et al. (2014). In order to improve this representation, a rime mass distribution is introduced in DESCAM for the last 27 bins of the 39 existing ones describing the ice particle number. Rime properties of the small ice particles (< 32 μm) were ignored since the lower size threshold for ice particles at which droplet collection begins ranges from 35 to 200 μm (Wang and Ji, 2000). It is therefore supposed that small ice particles are not influenced by rime.

From the introduction of the rime mass distribution, the last 27 bins of the ice particles can be characterized in terms of rime mass fraction, defined as $\phi = \frac{m_r}{m}$ with m the total mass and m_r the rime mass of the ice particle. Based on the 'fill-in' consideration introduced by Heymsfield (1982), the diameter of ice particle D (in cm) is defined as

$$D = \max\left[\left(\frac{m(1-\phi)}{\alpha}\right)^{\frac{1}{\beta}}, D_{gr}\right] \tag{2}$$

with D_{gr} the graupel diameter (in cm) defined by $D_{gr} = \left(\frac{m}{\alpha_{gr}}\right)^{\frac{1}{\beta_{gr}}}$ with α_{gr} = 0.034 and β_{gr} = 2.59 two coefficients taken from Heymsfield et al. (2018) and m the ice particle mass (in g). The α and β are the two coefficients previously defined for Eq. 1. When graupel particles are larger than 5 mm diameter, they are considered as hail, with α_{gr} = 0.111 and β_{gr} = 4.13. The 'fill-in' concept considers that rime fills the interstices of ice particles without increasing their size. Consequently, in Eq. 2, the term $m(1-\phi)$ corresponds to the vapor-grown mass, which determines the particle size. Furthermore, as expressed by Eq. 2, when the particle diameter D reaches the graupel diameter D_{gr}, the 'fill-in' process ceases and the particle interstices are assumed to be fully filled by rime. At this stage, for any increase of rime mass, the ice particle will follow the $m-D$ relation of Heymsfield et al. (2018) for graupel particles

The previous considerations are illustrated by Fig. 1 which depicts the size (D) of the ice particles in DESCAM as a function of their total mass (m) and rime fraction (ϕ). In this figure, for a given mass, the particle size can vary by a factor of 2, highlighting the significant effect of riming on the ice particles properties.

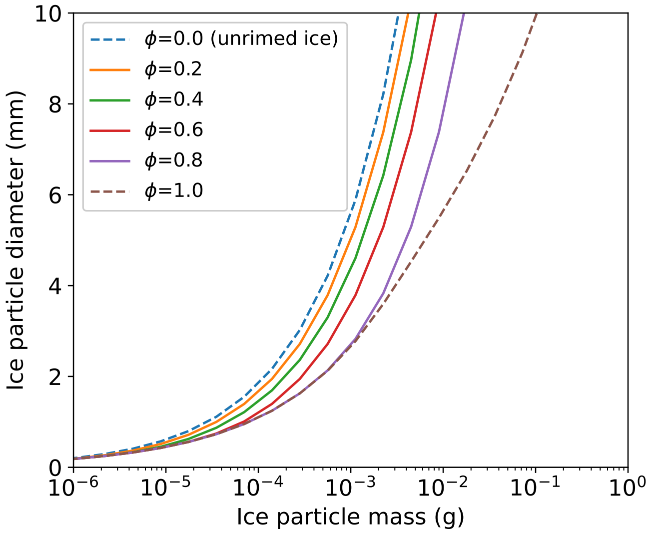

Figure 1. Mass - diameter relation of the ice particles in DESCAM depending on the rime fraction ϕ based on the 'fill-in' concept of Heymsfield (1982) and Morrison and Grabowski (2010).

2.3 Terminal velocity of ice particles

While the size of ice particles can change smoothly depending on their riming degree, their shape is not explicitly represented in DESCAM and is assumed to be spherical when shape is required in calculation. To calculate the terminal velocity of 115 ice particles from their size and mass without supposing any predefined shape, a common approach relies on dimensionless numbers that describe the aerodynamics of ice particles. The Best number, X and the Reynolds number, Re were introduced by Abraham (1970) to describe the drag coefficient of a sphere and were extended by Böhm (1989) for ice particles. Based on the same considerations, different parameterizations have been proposed in the literature (Mitchell, 1996; Khvorostyanov and Curry, 2002, 2005; Mitchell and Heymsfield, 2005). The parameterization used in DESCAM is that of Heymsfield and 120 Westbrook (2010) which provides a modification of the Best number X and Reynolds number Re defined by:

$$Re = \frac{\delta_0^2}{4}\left[\left(1+\frac{4\sqrt{X}}{\delta_0^2\sqrt{C_0}}\right)^{\frac{1}{2}}-1\right] \tag{3}$$

with C_0 = 0.35 the inviscid drag coefficient, δ_0 = 8.0 a dimensionless parameter and

$$X = \frac{\rho_a}{\nu^2}\frac{8mg}{\pi A_r} \tag{4}$$

with ρ_a the air density, ν the kinematic viscosity of air, m and D the ice particle mass and size and A_r the area ratio 125 of the ice particle defined by $A_r = \frac{A}{(\pi/4)D^2}$ with A the projected area. To calculate A_r, Heymsfield et al. (2002) proposed the following relation $A_r = 0.29D^{-0.18}$ based on measurements in tropical cloud anvils where ice crystals are assumed to be unrimed. For graupel particles, the area ratio is calculated from the projected area of graupel $A_{gr} = 0.625D^2$ given in Morrison and Grabowski (2010) (cgs units). Contrary to ice particle size, the projected area and the area ratio of rimed ice crystals is not provided by the ‘fill-in’ concept. However, since Eq. 4 depend on A_r, a smooth transition between the area ratios of unrimed and graupel particles is needed. Therefore, the area ratio of rimed ice particle is assumed to evolve linearly between those of graupel and unrimed ice particles as follows:

$$A_r^{rime} = A_r\left[1-\left(\frac{D_{gr}-D}{D_{gr}-D_{\phi=0}}\right)\right] + \frac{A_{gr}}{(\pi/4)D^2}\left(\frac{D_{gr}-D}{D_{gr}-D_{\phi=0}}\right). \tag{5}$$

with D the $D_{\phi=0}$ the diameter of unrimed ice particles (cgs units).

From the previous considerations, Fig. 2 shows the terminal velocity (V) of ice particles as a function of their size and rime mass fraction (ϕ). This figure also shows the graupel terminal velocities based on the velocity-diameter ($V-D$) relationships of Lee et al. (2015) and Heymsfield et al. (2018) that can be compared with those calculated for DESCAM. For graupel particles smaller than 1 mm diameter, the predicted terminal velocity in DESCAM aligns closely with Lee et al. (2015), whereas for larger particles it is closer to Heymsfield et al. (2018). This could be explained by the fact that graupel can have different densities in nature while it is currently not the case in DESCAM scheme. A possible future perspective would be to predict the volume of rime, as proposed by Morrison and Milbrandt (2015) which would allow rimed particles to have different densities and consequently gets rid of the fixed mass-diameter relation of graupel particles.

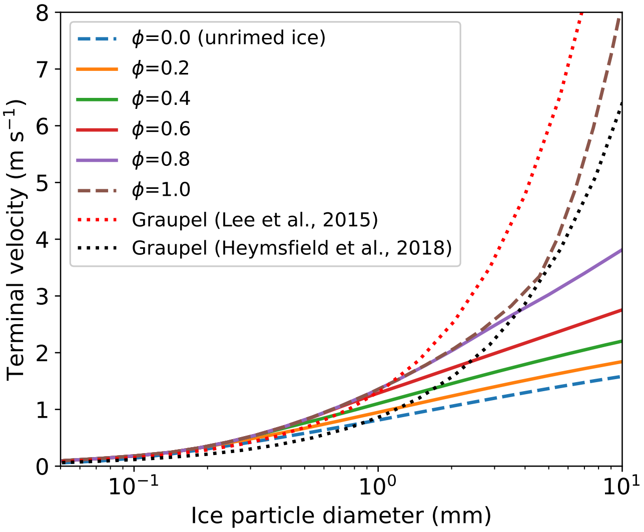

Figure 2. Terminal velocity of ice particles in DESCAM as a function of rime fraction ϕ, based on Heymsfield and Westbrook (2010) study. Dotted lines represent the graupel velocity-diameter ($V-D$) relationships from Lee et al. (2015) and Heymsfield et al. (2018).

2.4 Riming collision kernels

To represent the riming process in models, a key parameter is the collision kernels that quantify the rate at which two ice 145 hydrometeors collide per unit time and volume. From the mass, size and terminal velocity of the ice particles presented in Fig. 1 and Fig. 2, the collision kernels for a drop of mass m_1 and an ice particle of mass m_2 with rime fraction ϕ are defined by:

$$K(m_1, m_2, \phi) = \frac{\pi}{4}(D_1 + D_2)^2 |V_1 - V_2| E_c(m_1, m_2, \phi). \tag{6}$$

with V_1 and V_2 the terminal velocity of liquid drop (derived from Beard, 1976) and ice particles, respectively. E_c is the collision efficiency of riming which depends on the particles properties. For unrimed ice particles collecting liquid drops ($V_2 > V_1$), E_c 150 is derived from Wang and Ji (2000), while for graupel particles it follows the study of Cober and List (1993). For large liquid drops collecting ice particles ($V_1 > V_2$), the collision efficiencies are calculated from Lew et al. (1985). Therefore, for partly rimed particles, E_c is interpolated according to the particle size as done for A_r in Eq. 5.

The collision kernels are presented in Fig. 3a and Fig. 3b for unrimed and graupel particles. In both cases, the onset of riming occurs from drop or ice particles of around 100–200 μm diameter, as found by Lew et al. (1985) and Wang and Ji (2000). Fig. 155 3a shows an asymmetry in collision kernels due to the fact that drops fall faster than unrimed ice particles. In contrast, Fig. 3b shows a reduced asymmetry (except for large particles), as graupel particles have terminal velocities closer to those of liquid drops. This difference in terminal velocity also results in higher values of collision kernels for graupel compared to unrimed ice particles.

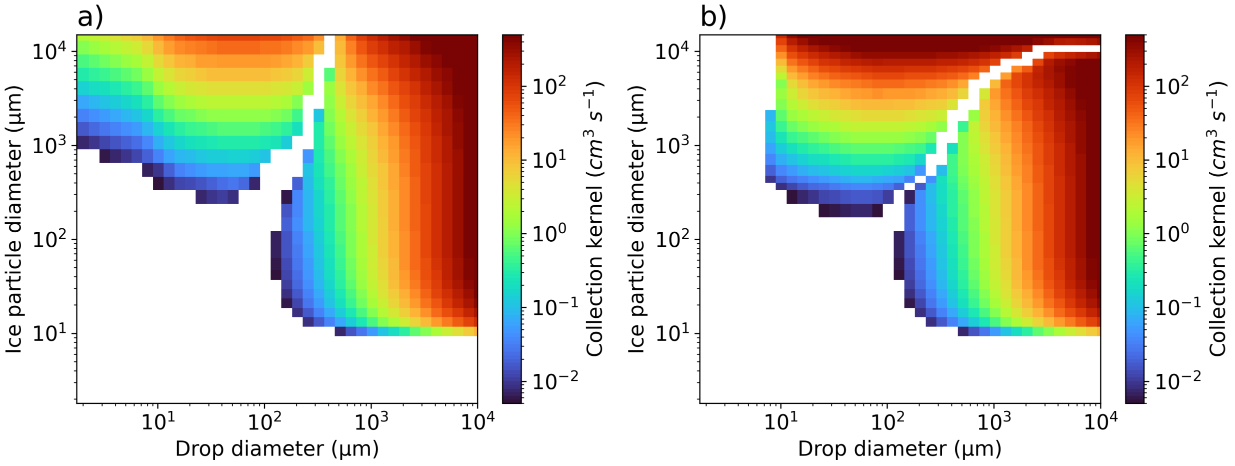

Figure 3. Riming collision kernels between liquid drops and ice particles, calculated using Eq. 6, that are implemented in DESCAM. Panel a) shows the kernels for unrimed ice crystals and panel b) presents those of graupel particles.

2.5 Budget equation for the rime mass distribution

The implementation of the rime mass distribution follows the same concepts and methodology as the track of aerosol mass inside ice particles and droplets developed and described by Flossmann and Wobrock (2010). The newly predicted rime mass distribution, is affected by various dynamical and microphysical processes:

$$\frac{\partial g_r(m)}{\partial t} = \left(\frac{\partial g_r(m)}{\partial t}\right)_{dyn} + \left(\frac{\partial g_r(m)}{\partial t}\right)_{nucl} + \left(\frac{\partial g_r(m)}{\partial t}\right)_{rim} + \left(\frac{\partial g_r(m)}{\partial t}\right)_{agg/brk} + \left(\frac{\partial g_r(m)}{\partial t}\right)_{dep} + \left(\frac{\partial g_r(m)}{\partial t}\right)_{sub} + \left(\frac{\partial g_r(m)}{\partial t}\right)_{melt} \tag{7}$$

The the left-hand term of Eq. 7 represents the total variation in rime mass $g_r(m)$ for an ice particle of mass m, due to the the sources and sinks generated by the microphysical processes. The effect of transport and sedimentation of ice particles is expressed by the the first term on the right-hand side of Eq. 7. As expressed by the second term on the right-hand side of Eq. 7, we also consider frozen drops generated by nucleation following Hiron and Flossmann (2015) method (i.e., condensation, immersion freezing, and homogeneous nucleation) as a source of rime. The third term represents the variation in rime mass caused by the collision of ice particles with liquid drops and is expressed as:

$$\left(\frac{\partial g_r(m)}{\partial t}\right)_{rim} = g_d(m_1)g_i(m_2)\frac{K(m_1,m_2,\phi)}{m_2} + g_d(m_1)g_r(m_2)\frac{K(m_1,m_2,\phi)}{m_1}. \tag{8}$$

with g_i the total ice mass distribution, g_d the liquid drop mass distribution and $K(m_1,m_1,\phi)$ the riming collision kernel presented in Fig. 3. The first term of the right-hand part of Eq. 8 expresses the gain of newly formed rime mass for an ice particle of mass m due to the collision between drops of mass m_1 with ice particles of mass m_2 having a rime fraction ϕ. Furthermore, as ice crystals grow by riming, their total mass is transferred to larger bins. Consequently, the initial rime mass of the colliding ice particle (m_2) must also be redistributed into larger bins. This effect is taken into account by the second term of Eq. 8, which considers the transport of pre-existing rime mass. Since the mass gained from the collision (m_1,m_2) does not necessarily fit the defined mass bin m, the redistribution method of Bott (1998) for the stochastic collection equation is applied.

Although aggregation does not change the total rime mass, it can redistribute it across different bins, depending on the combined rime masses of the colliding particles (fourth right-hand part term of Eq. 7). The transport of rime due to the aggregation of two ice particles is treated similarly to riming (second term of the righ-hand part of Eq. 8). Furthermore, when ice particles does not stick but break, the rime mass fraction of the parent particle is kept constant. Additionally, the loss of rime mass due to fragmentation is considered.

Similarly to riming, when a particle gains mass through vapor deposition (fifth term of Eq. 7), it is necessary to transfer the rime mass of the initial particle into larger bins. Therefore, the gain or loss of rime mass is set to be proportional to the number of ice particles growing (or shrinking) to larger (or smaller) bin during vapor growth (or sublimation), as is detailed in Appendix A.

The sixth term of Eq. 7 represents the loss of rime mass through sublimation. Since there is no information about the surface properties of the ice particles (i.e. consisting of rime or vapor-grown ice), we assume that the particle rime fraction ϕ remains

https://doi.org/10.5194/egusphere-2025-3202
Preprint. Discussion started: 14 October 2025

constant during sublimation. As a result, the rime mass decreases in the same proportions as for the total ice mass. Finally, the last term of Eq. 7 expresses the sink of rime mass due to melting of ice particle (which is set to occur instantaneously, contrary to Planche et al., 2013a).

To ensure the correct transport of rime mass through the binned distribution, numerical tests were conducted by using predefined rime mass distributions for each process included in Eq. 7 (with transport of sedimentation turn off). Similar tests of rime transport during depositional growth, aggregation and riming are presented in Morrison and Grabowski (2010) (their Figs. 1,2 and 4).

3 Simulation case

This study focuses on the snowfall event that occurred between 7 and 9 March 2018, during the passage of a low-pressure system over the Korean Peninsula during the ICE-POP 2018 campaign. This event is categorized as "warm low" according to Kim et al. (2021), following the synoptic classification of Jeoung et al. (2020). The "warm low" system forms over the southwestern part of the Korean Peninsula due to the abundant moisture supplies from the East China Sea. This moisture leads to the development of precipitating cloud systems moving across the peninsula and producing heavy snowfall. After the passage of the low pressure deep system, the wind in the upper layer shifts from southwest to northeast, bringing in dry air. Consequently, a shallower cloud system forms exclusively in the lower layer. This system is mainly influenced by moisture from the East Sea, driven by sea-air interactions and orographic lifting along the eastern mountainous coastal region. More details on this type of cloud system can be found in Kim et al. (2021).

3.1 Observations

Observations were conducted at several measurement supersites equipped with ground-based microphysical probes, wind profilers, radars, and both fixed and mobile radiosounding stations. An overview of the instrumentation of the ICE-POP 2018 campaign can be found in Kim et al. (2021); Gehring et al. (2021, 2020b); Tsai et al. (2022). The present study mainly uses the instrumentation of the MHS (Mayhills supersite; 37.6652° N, 128.6996° E; 789 m altitude) station. This site includes a vertically pointing X-band radar and a W-band cloud Doppler radar, both providing radar reflectivity. A OTT Pluvio^2 rain gauge is used to measure the rainfall accumulation and intensity and an OTT Parsivel^2 disdrometer (Tokay et al., 2014) is used to determine the dominant type of precipitation (rain or snow). The Particle Imaging Package (PIP, Newman et al., 2009; Pettersen et al., 2020) probe provides the size distribution of ice particles from 0.1 to 26 mm diameter. Complementary, a multi-angle snowflake camera (MASC, Garrett et al., 2012) is used to obtain the morphological properties of the ice particles following Praz et al. (2017) method, providing a rime index (ranging from 0 to 1) and a classification in 6 hydrometeors types. In addition, three other disdrometers and rain gauges, deployed at YPO (Yongpyong Observatory; 37.6433°N, 128.6705°E; 772 m altitude), BKC (Bokwang-ri Community Center; 37.7381°N, 128.8058°E; 175 m altitude), and GWU (37.7709°N, 128.8669°E; 36 m altitude) are used in this study to provide the precipitation properties previously mentioned.

Fig. 4a shows the locations of the measurement sites mentioned previously, within the third (most refined) domain of DESCAM model. The YPO and MHS sites are located in mountainous regions while BKC and GWU are close to the coast (i.e. at lower altitudes).

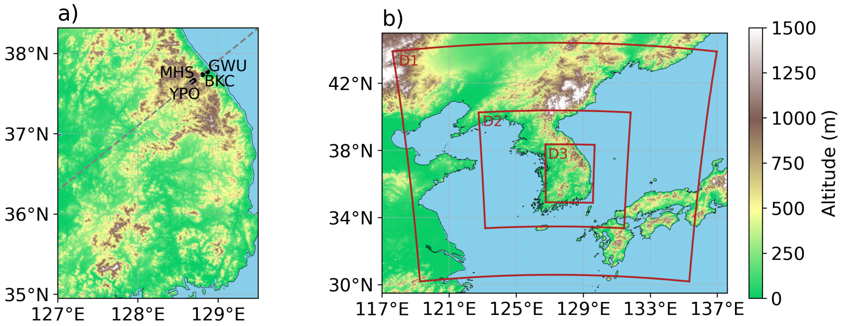

Figure 4. a) Location of the measurement sites of the ICE-POP 2018 campaign indicated in the innermost model domain. b) Nested model domains of DESCAM considered for the numerical experiments with 8 km (D1), 4 km (D2) and 1 km (D3) horizontal resolution.

3.2 Numerical experiment

In this study, the bin microphysics scheme DESCAM (see sections 2.1 and 2.2 for more details) included in the 3D dynamical frame of Clark et al. (1996); Clark (2003) is used. The numerical experiment consists of three nested domains shown in Fig. 4b, composed of 193 × 193, 193 × 193 and 258 × 386 grid points corresponding to horizontal resolutions of 8, 4 and 1 km, similar to the setup of Park et al. (2024). The vertical resolution is set to be non-equidistant with around Δz = 40 m at ground level and Δz = 230 m at 9 km. The simulations are run for two days from March 7, 2018 at 00:00 UTC to March 9, 2018 at 00:00 UTC with a time step Δt = 4 s. The initial and boundary conditions of DESCAM are taken from ERA 5 ECMWF reanalysis (Hersbach et al., 2020). The aerosol particle size distribution is derived from the measurements of Yum et al. (2007) at Jeju Island (during March–April) and Park et al. (2021) at Baengnyeong Island, for air masses coming from the East China sea (classified as Type II and III in the aforementioned studies) which is where the cloud system forms. Therefore, the total aerosol particle concentration is set to 4500 cm^{-3} at ground and is assumed to decrease exponentially to 1500 cm^{-3} for altitudes above 3 km. We presumed that aerosol particles are composed of ammonium sulfate.

Two simulations were conducted using DESCAM. The first one, mentioned as the "control" simulation, includes the recent implementations described in Section 2.1, with the predicted rime mass distribution, the fill-in effect, and the rime dependency of ice particle terminal velocity and collision kernels. The second simulation, called "no rime", disables the predicted rime scheme and follows the original configuration of DESCAM before the new developments.

4 Results

The ability of the DESCAM (control simulation) to reproduce the observed cloud system evolution and intensity is evaluated in Section 4.1. The effect of the predicted rime mass distribution on the precipitation accumulation and evolution is examined in Section 4.2. Section 4.3 focuses on the analysis of ice particle properties (size, number, and rime content) to assess the relevance of the updated version of DESCAM. Finally, Section 4.4 investigates how the dynamical configuration influences the microphysical properties of the ice particles.

4.1 Cloud system intensity and evolution

The temporal evolution of the X and W band radar reflectivity at the MHS mountainous station is shown in Fig. 5 for both ground observations and the DESCAM control simulation. The modeled reflectivity is calculated using the Self-Similar Rayleigh–Gans Approximation (SSRGA) method (Hogan et al., 2017; Leinonen et al., 2017), that account for the internal structure of ice aggregates. The ice particle properties for this method follow the SSRGA-LS15-B0.2 configuration described by Tridon et al. (2019), that provides the best agreement with observed reflectivity measurements. As shown in Fig. 5a and c, the radar observations show two distinct cloud systems with a deep system induced by the low pressure passage until 6:00 UTC (March 8), followed by a shallower one. The deep low pressure system produces precipitation at the surface from around 09:00 UTC, whereas in DESCAM (Fig. 5b,d) the precipitation onset is delayed until 15:00 UTC. Nevertheless, the model accurately reproduces the observed weakening of reflectivity around 18 UTC, suggesting that the simulation does not exhibit a systematic delay but rather fails to reproduce the early development phase of the low pressure system between 09:00 and 15:00 UTC.

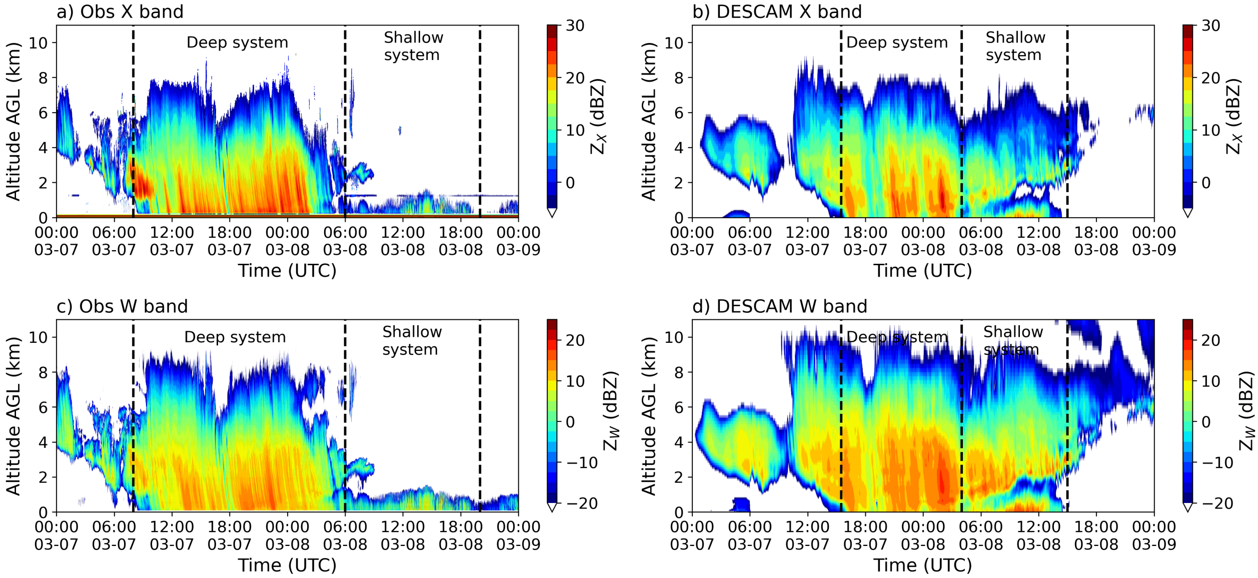

Figure 5. Time-height (above ground level) evolution of radar reflectivity at the MHS station: a) X-band observations, b) DESCAM X-band control simulation, c) W-band observations, and d) DESCAM W-band control simulation. Dashed lines indicate the limits of the different cloud systems.

Around 06:00 UTC (March 8), radar observations (Fig. 5a and c) show the transition of the deep low pressure system to a shallower one of around 2 km height above ground level. This system, as explained in Section 3, corresponds to the dominance of an easterly low level flow following the low pressure system, inducing orographic lifting and the formation of low level clouds. In Fig. 5b and d, although the model reproduces the presence of a shallow system of 2 km height, it also generates a second cloud layer above 2 km altitude that is absent in the observations. Therefore, the transition of these two cloud systems is less distinct in DESCAM than in the observations. Additionally, the shallow system starts slightly earlier in the simulation compared to the observations and consequently ends 5 hours earlier, around 15:00 UTC on March 8. The difference between the X and W band radar reflectivities is illustrated by the dual wavelength ratio reflectivity (DWR i.e. Z_X–Z_W) in Fig. A1 of Appendix B.

To further evaluate the intensity and vertical structure of radar reflectivity, Fig. 6 and 7 present the vertical frequency distribution of observed and simulated reflectivity at X and W bands for the two distinct cloud systems. For the deep system, DESCAM control simulation (Fig. 6b and d) shows high reflectivity frequencies near 20 dBZ (X band) and 10 dBZ (W band) next to the surface, matching well the intensity of the observations (Fig. 6a and c). Moreover, compared to the observations, the vertical decrease in reflectivity frequency is well captured in the simulation for both X and W bands. As mentioned in Kim et al. (2021), the presence of higher reflectivity with decreasing altitude is due to the growth of snow aggregates. However, in Fig. 6d, for the W band, the modeled reflectivity extends to higher altitudes, reaching a maximum frequency of –12 dBZ at approximately 9 km, compared to 8 km in the observations.

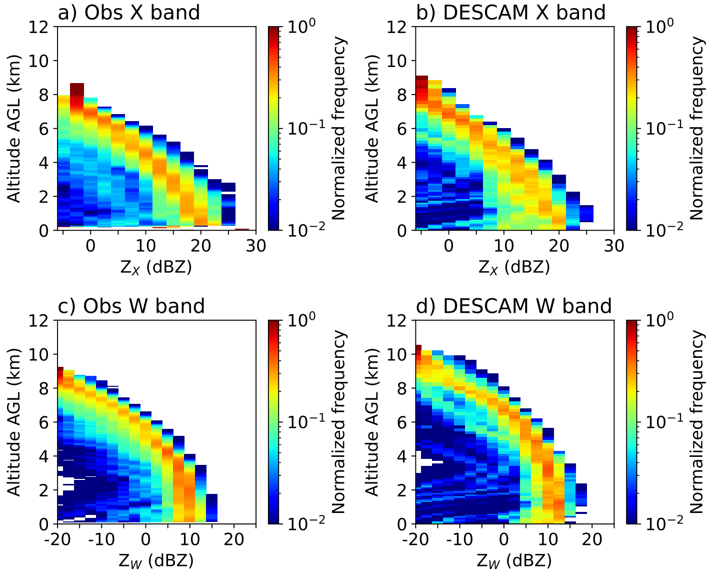

Figure 6. Frequency of radar reflectivity as function of the altitude above ground level for the deep cloud system presented in Fig. 5 with: a) X-band observations b) X-band DESCAM control simulation c) W-band observations and d) W-band DESCAM control simulation.

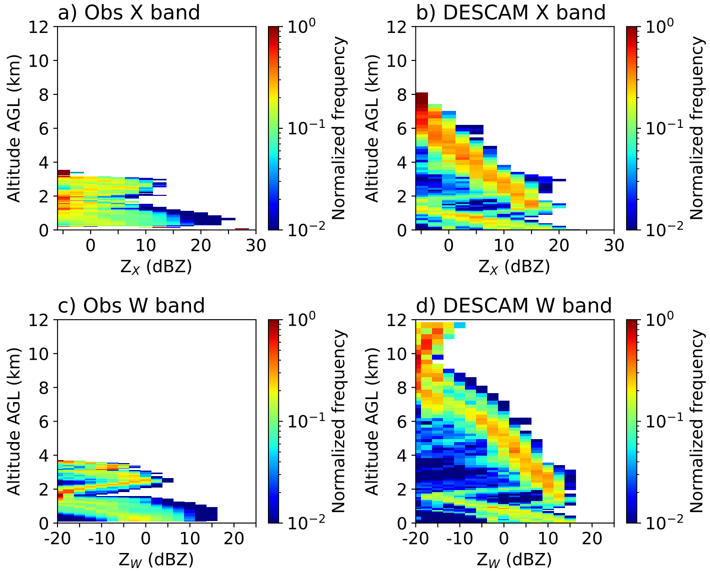

Figure 7. As Fig. 6 but for the shallow cloud system presented in Fig. 5.

For the shallow system, radar observations (Fig. 7a and c) display reflectivity frequencies at the surface ranging from 0 to 15 dBZ for the X band and –10 to 10 dBZ for the W band. In contrast, DESCAM (Fig. 7b and d) overestimates the reflectivity intensity throughout the shallow layer, with a consistent positive bias of approximately +5 dB for both bands and for altitudes lower than 2 km height. Nevertheless, the general vertical decrease in reflectivity up to 2 km is reasonably well captured.

Above 2 km, substantial discrepancies emerge in Fig. 7 as the model continues to simulate high reflectivity values (from 10 dBZ at 2 km down to –10 dBZ at 8 km), similarly as the structure of the earlier deep system (Fig. 6). In contrast, the observations show much weaker reflectivity above 2 km. These differences suggest that the model may be prolonging the presence of the upper portion of the deep system, leading to an upper cloud layer above the shallow system.

Fig. 8 shows the W-band mean Doppler velocity for the observations and DESCAM control simulation. During the deep cloud system, the observed Doppler velocity near the ground is close to -1 m s^{-1}, which is accurately reproduced by the model, showing similar values with only some peaks reaching around -1.3 m s^{-1}. Between 4 and 6 km altitude, radar observations (Fig. 8a) shows an increase in Doppler velocity up to –2 m s^{-1}. As mentioned in Gehring et al. (2020b) and Kim et al. (2021), this enhancement may be attributed to a shear layer and therefore turbulence that leads to favor aggregation and riming. However, this rise in Doppler velocity also coincides with temperatures near –15°C, that favor dendritic growth and aggregation, potentially resulting in larger and faster falling ice particles. However, as the DWR, which is sensitive to ice particle size, does not significantly rise at this altitude (Fig. A1, Appendix B), the large Doppler velocities of Fig. 8a can be more likely attributed to riming rather than aggregation.

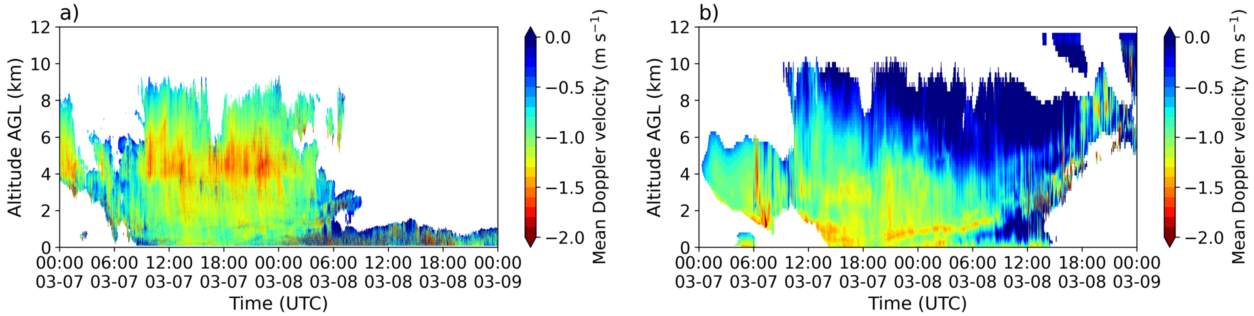

Figure 8. Mean Doppler velocity (defined positive upwards) at the MHS station for a) W-band radar observations in and b) DESCAM control simulation. Data are presented for reflectivity values exceeding –20 dBZ (see Figs. 5c,d).

Regarding the control simulation (Fig. 8b) the most notable increase in modeled velocity occurs near 1.5 km, within a transition layer between easterly and southwesterly airflows, where wind shear and thermal inversion are present. Close to 3.5 km, only a slight increase in Doppler velocity is provided by the model with much lower values than in the observations. Above 6 km, despite accurately representing radar reflectivity in Fig. 5, DESCAM significantly underestimates the Doppler velocity compared to the observations. This discrepancy suggests that DESCAM may generate an excessive number of small ice particles in the upper cloud layers. Indeed, while these particles can produce reflectivity intensities comparable to the observations in Fig. 5, their low terminal velocity leads to an underestimated Doppler velocity in Fig. 8. The significant underestimation of DWR by the simulation compared to radar observations in Fig. A1 (Appendix B) further confirms that DESCAM underestimates ice particle sizes near the cloud top.

In Fig. 8a, during the shallow cloud phase and below 2 km altitude, the observed Doppler velocities show a large variability, ranging from 0 to –2 m s^{-1}, whereas the modeled Doppler velocities appear more uniform, with values around –1 m s^{-1}. Additionally in Fig. 8b, the modeled cloud layer above 4 km after 06:00 UTC (March 8) exhibits relatively low Doppler velocities (–1 to 0 m s^{-1}) that are associated with significant reflectivity (5b,d). This further indicates the presence of numerous small, and slowly precipitating ice particles, similarly to the results for the upper levels of the deep system mentioned previously.

The overproduction of these small ice particles likely originating from a numerical artifact. In the southwestern and northwestern corners of the outermost domain, mountainous terrain near the boundaries (Fig. 4b) appears to influence incoming air masses by generating artificial updrafts at the upper levels of the domain. These updrafts lead to an artificial humidity enhancement at the western lateral boundary, triggering the production of a large number of ice particles by heterogeneous and homogeneous ice nucleation.

4.2 Precipitation properties

The temporal evolution of accumulated precipitation at the four observation stations, based on Pluvio measurements and compared with DESCAM simulations, is shown in Fig. 9. As already observed for radar reflectivity (Fig. 5), the first phase of the cloud system is not represented by the model, with precipitation beginning around 15:00 UTC in the simulation, which is 3 hours later than in the observations. After this delay, precipitation rate from the control simulation becomes comparable to observations in the coastal regions (Fig. 9c,d), but remains slightly lower in the mountainous areas (Fig. 9a,b). Due to a later start, at the end of the deep system (04:00 UTC on March 8), the accumulated precipitation in DESCAM control simulation is less than half of the Pluvio measurements in mountainous areas (Fig. 9a,b) and about 5 mm lower in coastal areas (Fig. 9c,d).

https://doi.org/10.5194/egusphere-2025-3202
Preprint. Discussion started: 14 October 2025

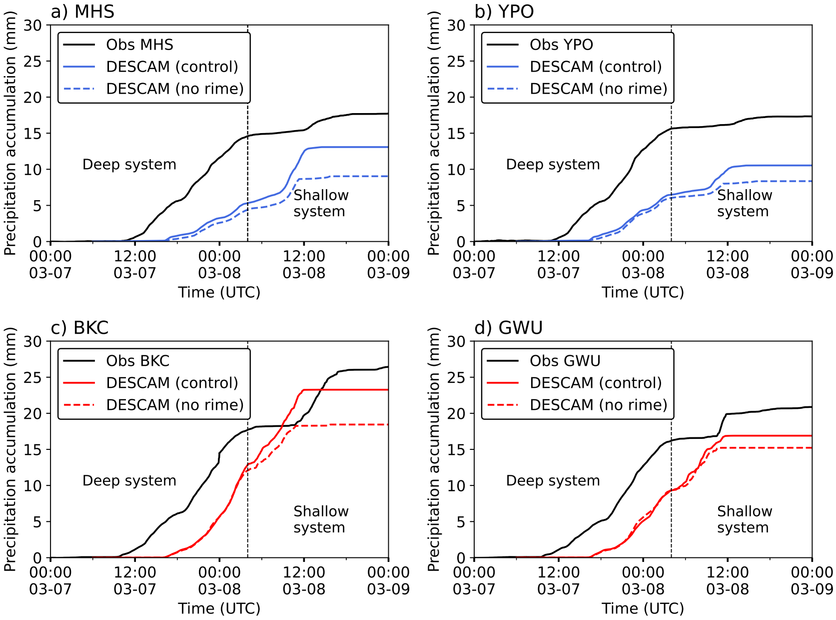

Figure 9. Temporal evolution of the precipitation accumulation at MHS, YPO, BKC, and GWU stations. Black lines represent observations from the Pluvio rain gauge, while blue and red lines show DESCAM simulation results a) - b) for mountainous stations and c) - d) for coastal stations. Plain and dashed lines represent DESCAM results for the control simulation and no rime simulation, respectively. The black dashed line indicate the limits of the different cloud systems.

Due to a delayed onset, the accumulated precipitation in the control simulation after the passage of the deep system (around 4 UTC on March 8) is roughly half of the observed total in mountainous areas, and about 5 mm lower in coastal regions.

For the shallow system, in the mountainous regions (Fig. 9a,b), DESCAM control simulation leads to more intense precipitation, that starts 3 hours earlier (at 09:00 UTC on March 8) compared to the observations (at 12:00 UTC on March 8). This aligns with the +5 dB bias in the modeled radar reflectivity shown in Fig. 7 for the MHS station. This stronger modeled shallow system compensates the earlier underestimation of precipitation accumulation. At the coastal sites (Fig. 9c,d), DESCAM control simulation produces similar precipitation rate as the observed one while it starts immediately after the deep system, whereas observations show a distinct gap of 6 hours between the two events. Overall, at the end of the control simulation, DESCAM underestimates total precipitation accumulation by about 5 mm at all sites compared to the Pluvio observations.

In Fig. 9, the comparison between the control and no rime simulation highlights the significant role of riming in precipitation formation. Turning off the predicted rime scheme results in a reduction of precipitation at all stations, with differences up to 5 mm (i.e. around 17% to 40%) at 00:00 UTC on March 9. These discrepancies are most notable at the end of the deep system and during the shallow phase that are periods when riming is especially active.

To further evaluate the precipitation characteristics simulated by DESCAM, Fig. 10 presents the temporal evolution of precipitation accumulation type (for > 0.1 mm accumulation within 3 hours) at the four observation stations. At the two MHS and YPO mountainous stations (Fig. 10a and c), Parsivel data indicate that ice particles dominate precipitation during the deep cloud system phase. This observation is consistent with DESCAM results (Fig. 10b and d), which also show predominantly ice precipitation. For the shallow cloud system, both observations and the model show the occurrence of a small amount (i.e. less than 20%) of liquid precipitation.

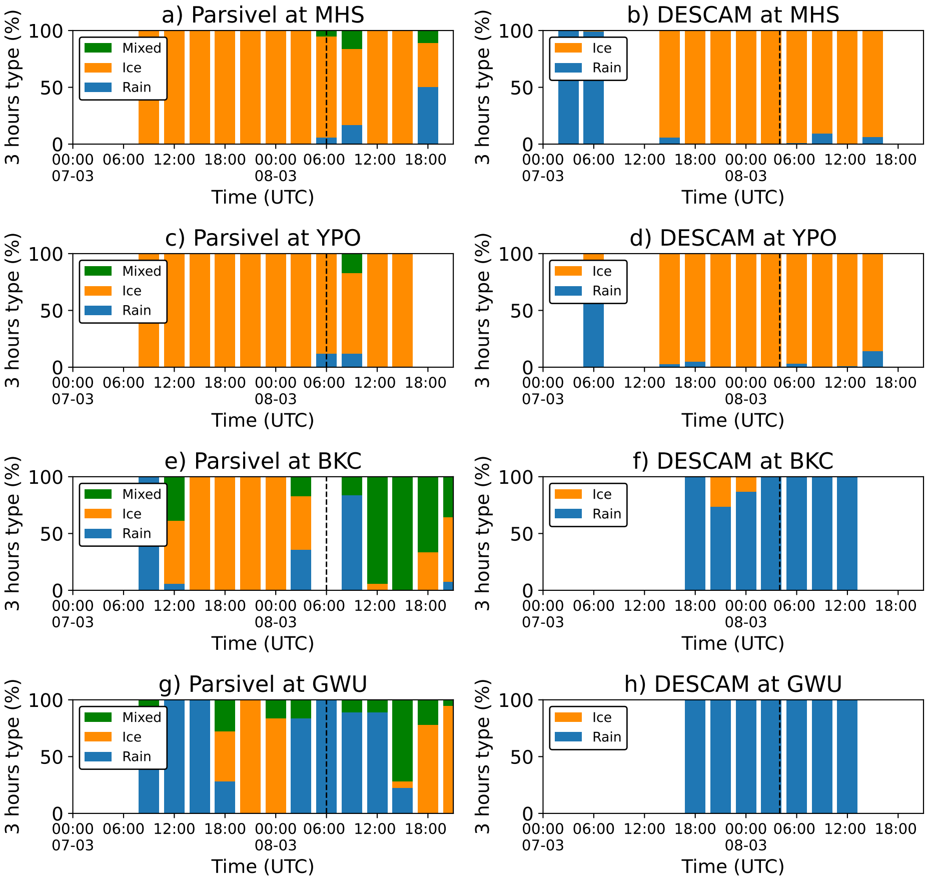

Figure 10. Temporal evolution of precipitation accumulation type (for > 0.1 mm within 3 hours) based at the MHS, YPO, BKC, and GWU stations observed by the Parsivel instrument (left column) and simulated by DESCAM (right column) for the control simulation. The 'mixed' particles describes melted or melting hydrometeors not identifiable as either rain or snow. The black dashed line indicate the limits between the deep and shallow cloud systems.

In contrast, for the BKC and GWU coastal stations, the model outputs (Fig. 10f and h) give almost exclusively liquid precipitation, with only a minor contribution from ice particles at BKC. However, the Parsivel observations in Fig. 10e and g shows a significant part of ice precipitation during the deep system and a transition to mixed-phase (partially melted) particles during the shallow system.

This suggests that DESCAM may overestimate the altitude of the melting layer in coastal regions. Another possible cause of the liquid overestimation in DESCAM is maybe due to the assumption that ice particles melt instantaneously at the 0°C isotherm level. In reality, melting is gradual, potentially prolonging the presence of solid or mixed-phase particles, as suggested by the Parsivel observations.

Fig. 11 presents the spatial distribution of accumulated precipitation at the end of the simulation, for ice (Fig. 11a), rain (Fig. 11b), and total precipitation (Fig. 11c). As shown in Fig. 11b, ice precipitation is restricted to the mountainous coastal regions in the northeast region of the domain which is consistent with the results presented in Fig. 10. It should be noted that the BKC station is located in the transition zone between areas dominated by ice and those dominated by rain (Fig. 11a). The rest of the domain (especially in southwest) is largely influenced by liquid precipitation. Figure 11c also highlights that precipitation exceeds 30 mm in the southwest part of the domain, where the deep system comes from.

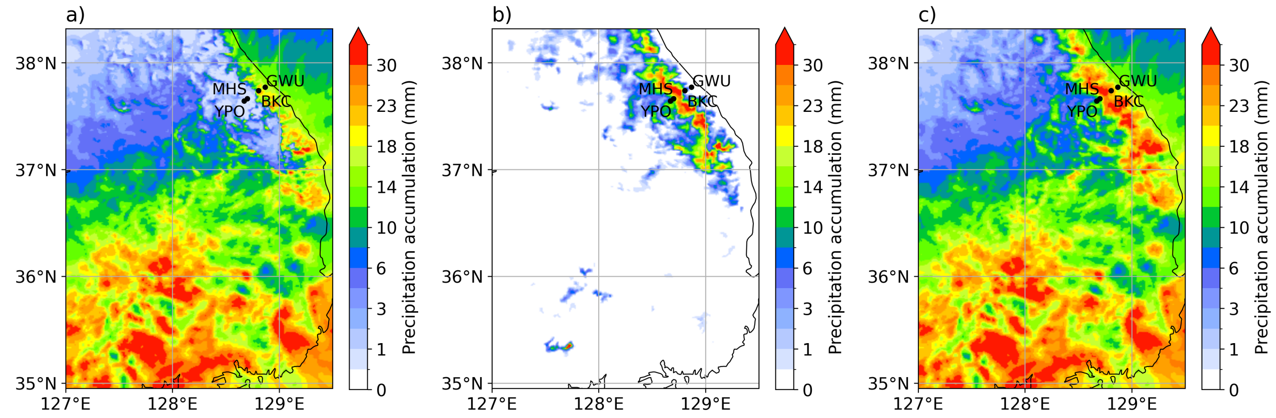

Figure 11. Precipitation accumulation from DESCAM control simulation within the innermost domain at the end of the event (00:00 UTC March 9), for a) liquid precipitation, b) ice precipitation, and c) total precipitation.

To further assess the impact of the predicted rime mass implementation, Fig 12 shows that it leads to a notable increase in precipitation accumulation, with differences of up to 10 mm. This is particularly the case for the southwestern part of the domain and the coastal mountainous regions close to the observation sites (consistent with Fig. 9). Overall, the total precipitation mass in the third domain increases by approximately 6.5% in the control simulation. However, a local reduction is present in the southeastern part of the domain. This reduction could be explained by the West to East movement of the deep system combined with the higher sedimentation velocities of rimed ice particles in the control simulation, that favors early precipitation in the western part of the domain. Although the majority of precipitation during this event is liquid (except for the mountainous regions; see Fig. 11b) predicted rime in DESCAM also induces an important effect on the liquid precipitation amount. This highlights the important role of the representation of ice particles properties in models which melt and contribute to liquid precipitation.

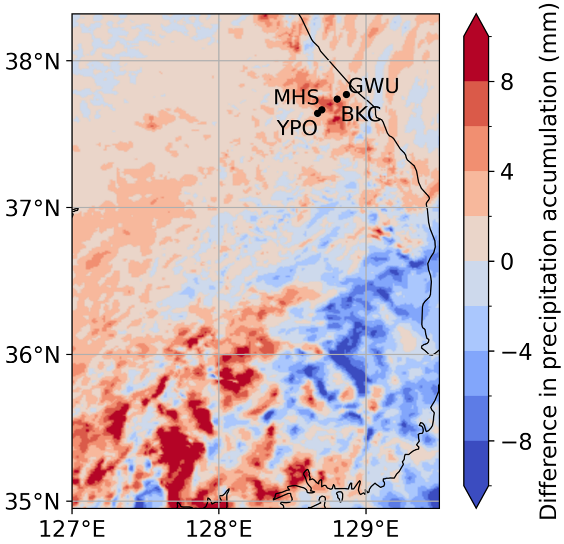

Figure 12. Difference between DESCAM control and no rime simulations for the total (liquid + ice) precipitation accumulation (at 00:00 UTC, on March 9). Positive (red) values indicate an increase in precipitation in the control simulation, while negative (blue) values indicate a decrease in the control simulations.

4.3 Ice particles properties

Fig. 13 presents the temporal evolution of the ice particle size distribution at the MHS station, given by the PIP probe (Fig. 13a) and by DESCAM control simulation (Fig. 13b) for particles larger than 100 μm. In Fig. 13b, before 15:00 UTC (March 7), both simulations produce small ice particles (< 1 mm) before the onset of precipitation whereas no ice particles are detected by the PIP (Fig. 13a) before 10:00 UTC. Furthermore, during the deep phase, DESCAM control simulation (Fig. 13b) produces a broader particle size distribution compared to observations, with a mean diameter fluctuating between 0.5 and 1.8 mm. In contrast, the PIP observations of Fig. 13a show a more steady mean diameter of around 0.8 mm. The model also displays a bimodal distribution before 00:00 UTC (March 8) contrary to the PIP observations. These discrepancies suggest that the current representation of ice particle aggregation in DESCAM, recently revised by Grzegorczyk et al. (2025a), still requires further refinement.

https://doi.org/10.5194/egusphere-2025-3202
Preprint. Discussion started: 14 October 2025

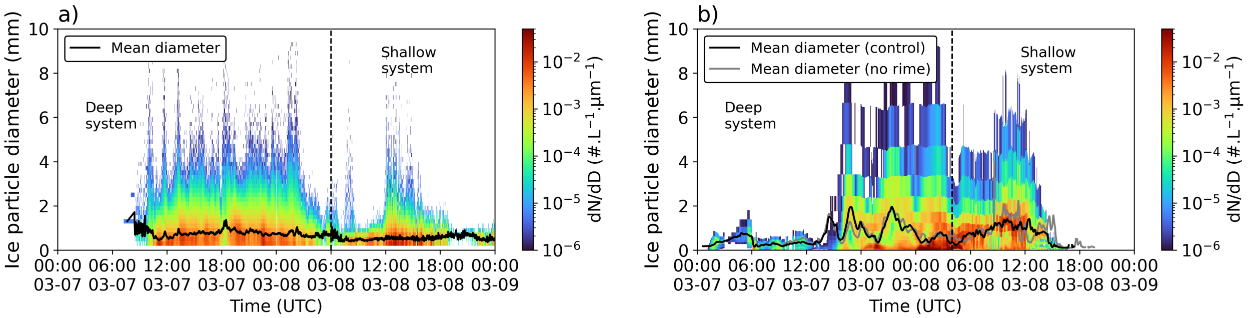

Figure 13. Temporal evolution of ground based observation of ice particle size distribution a) from the PIP instrument at MHS and b) given by DESCAM control simulation. Solid lines indicate the mean particle diameter. In panel b), the black line represents the number weighted mean particle diameter for the control simulation, while the gray line corresponds the no rime simulation. Only ice particle larger than 100 μm are considered. The black dashed line indicate the limits of the different cloud systems.

In the shallow cloud phase, PIP measurements (Fig. 13a) show smaller ice particle than in the deep system with a mean diameter around 0.5 mm. The control simulation, overestimates the size of the ice particles with a mean diameter around 1 mm. Interestingly, the no rime simulation generates even larger particles, of about 1.5 mm before 12:00 UTC (March 8). This shows that the implementation of the predicted rime distribution helps to mitigate the overestimation of large ice particles given by DESCAM.

The temporal evolution of the total number concentration of ice particles larger than 100 μm obtained from the PIP instrument and DESCAM control and no rime simulations is presented in Fig. 14. During the first part of the deep cloud system (i.e. between 15:00 and 00:00 UTC on March 7), both DESCAM simulations significantly underestimate the number of ice particles by around a factor two compared to observations. In contrast, during the second phase of the deep system (between 00:00 UTC and 06:00 UTC on March 8), both simulations, particularly the control, overestimate the particle number concentration, again by a factor of two.

https://doi.org/10.5194/egusphere-2025-3202
Preprint. Discussion started: 14 October 2025

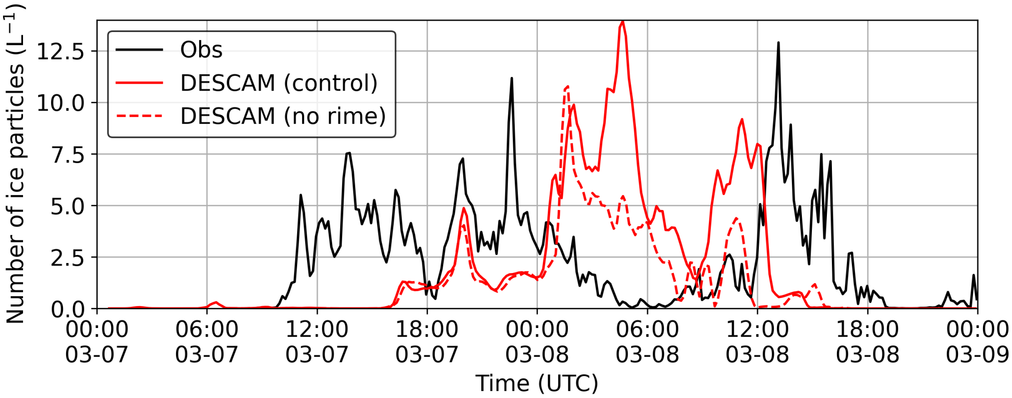

Figure 14. Temporal evolution of the number of ice particle (10-minute averaged) larger than 100 μm at MHS station, observed by the PIP instrument (black line) and simulated by DESCAM, with the control and no rime simulations shown in solid and dashed red lines, respectively.

During the shallow phase (from 06:00 UTC on March 8), the number of ice particles in the control simulation aligns well with PIP observations, while the no-rime simulation underestimates their concentration. These results further support that the predicted rime implementation leads to a more realistic representation of the ice particle properties during the shallow phase as seen for particle size in Fig. 13b.

To investigate the riming properties of ice particles, Fig. 15a shows the temporal evolution of the riming index derived from MASC images (Praz et al., 2017), as well as the simulated rime mass fraction from DESCAM control simulation. The rime mass fraction is defined as the ratio of rime mass to total ice mass of all particles larger than 100 μm (i.e. approximately the detection threshold of the MASC). While the riming index and rime mass fraction are different parameters, their temporal variation can be still compared to assess the model ability to represent the evolution of rime amount in ice particles. Figure 15b displays the number of particles, from the MASC images over 10-minute intervals, categorized in different hydrometeor types.

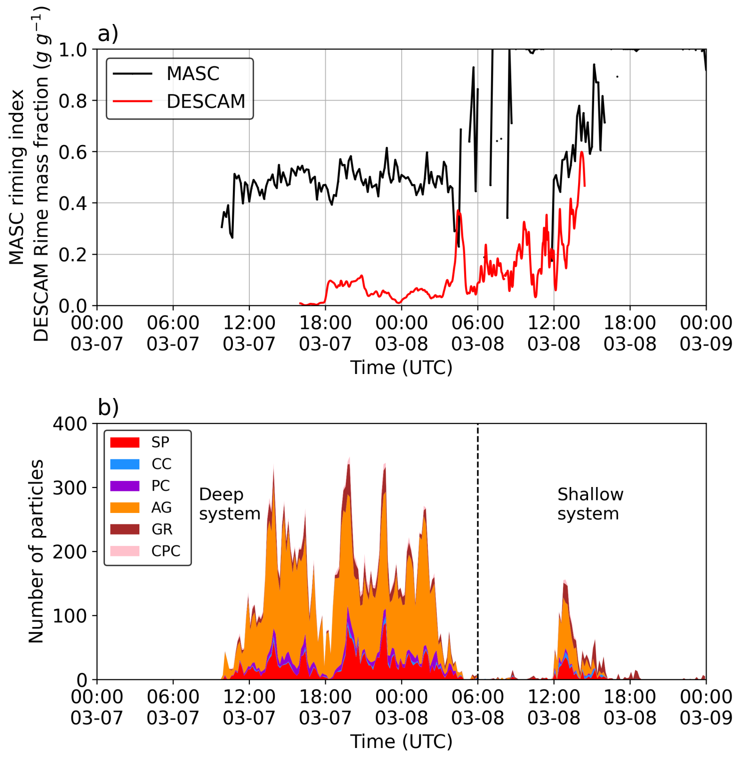

Figure 15. a) Evolution of the rime index retrieved from MASC observations, compared to the rime mass fraction from DESCAM simulation at MHS station. b) Number of particles (per 10-minute interval) for each hydrometeor species observed by MASC with: small particles (SP), columnar crystals (CC), planar crystals (PC), aggregates (AG), graupel (GR), and combinations of columnar and planar crystals (CPC). The rime index and hydrometeor classification are retrieved from Praz et al. (2017) method. The black dashed line indicate the limits of the different cloud systems.

In Fig. 15a, during the deep system (i.e. before 06:00 UTC), the MASC riming index remains close to 0.5, along with the presence of rimed aggregates (AG) (Fig. 15b). In comparison, DESCAM gives a rime mass fraction of approximately 0.1, suggesting a possible underestimation of rime amount during the deep phase.

At the end of the deep system, a peak is obtained for the simulated rime mass fraction around 04:00 UTC on March 8, coinciding with peaks in the MASC riming index (from 04:00 to 9:00 UTC on March 8). A second, more pronounced increase occurs at the end of the shallow system at 14:00 UTC on March 8, with the MASC riming index reaching 0.9 and the simulated rime mass fraction increasing at 0.6. These consistent trends suggest that the predicted rime mass distribution implemented in DESCAM reproduces well the evolution of the riming properties of the ice particles.

The particle types classified from the MASC images (Fig. 15b), along with the ice particle total number concentration (Fig. 14a), reveal that the riming index in (Fig. 15a) increases as the total number of ice particles decreases, while the number of graupel (heavily rimed) particles observed with the MASC remains relatively constant. This suggests that a higher proportion of the remaining particles are rimed. DESCAM reproduces well this trend, particularly between 12:00 and 14:00 UTC on March 8 (Fig. 14a), when an increase in rime mass fraction coincides with a decrease in ice particle number concentration. Despite that, it remains challenging to assess whether the amount of rime mass is accurately reproduced by DESCAM.

4.4 Riming event

To better understand the origin of the surge in rimed particle, Fig. 16 shows vertical cross sections from the DESCAM control simulation within the third domain. These cross-sections present the rime mass fraction, liquid water content (LWC), ice water content (IWC), relative humidity (RH), and the 2d wind field (along the dashed line of Fig. 4). They correspond to the deep system at 00:00 UTC on March 8 (Fig. 16a,d) and the shallow system at 14:00 UTC for the same day (Fig. 16c,d).

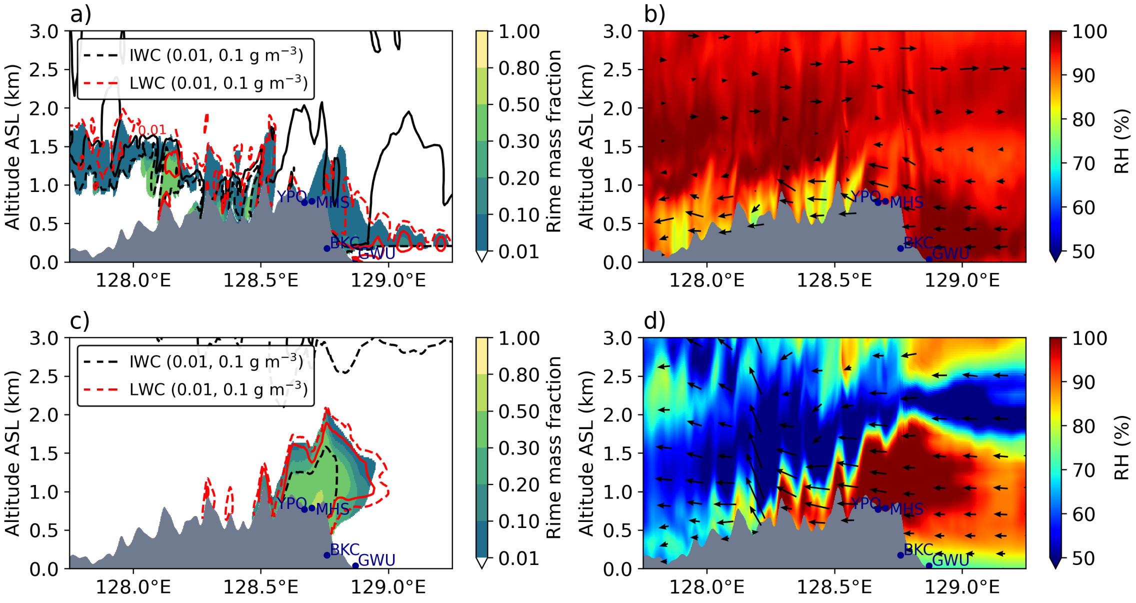

Figure 16. Vertical cross sections from DESCAM control simulation (along the dashed line of Fig. 4, passing through the measurement sites) within the innermost domain. Panels a) and c) show the rime mass fraction, with ice water content (IWC) and liquid water content (LWC) contours at 0.01 and 0.1 g m^{-3}, corresponding to the end of the the deep system (00:00 UTC, March 8) and the shallow system (14:00 UTC, March 8), respectively. Panels b) and d) present the relative humidity and the 2d wind field for the same time periods.

Fig. 16c highlights that, at the end of the shallow system, the rime fraction exceeds 0.5 at the mountainous stations (YPO and MHS), coinciding with high supercooled LWC (> 0.1 g m^{-3}) and low IWC (< 0.1 g m^{-3}). As shown in Fig. 16d, this cloud system seems to result from orographically induced updrafts lifting humid marine air brought by the easterly flow. The relatively low cloud top and the surface temperatures just below 0°C (not presented) over the mountainous terrain promote the persistence of supercooled liquid water. This therefore favors the formation of rimed particles, as reflected in DESCAM rime mass fraction (15a). The previous work of Kusunoki et al. (2005) has shown that terrain induced updrafts are promoting

https://doi.org/10.5194/egusphere-2025-3202
Preprint. Discussion started: 14 October 2025

the presence of supercooled liquid water and thus increase the riming process efficiency. It was especially the case at the measurement points of ICE-POP when northeasterly air flow becomes dominant, as mentioned by Kim et al. (2021).

In contrast, Fig. 16a,b depict the conditions during the deep cloud phase at 00:00 UTC (March 8). In this case, northeasterly winds are restricted below 1.5 km, whereas above, a dominant southwesterly flow associated with the low-pressure system transports snow aggregates over the mountainous regions. As a result, the amount of supercooled LWC for the deep system is reduced compared to Fig. 16c, particularly near the mountainous sites, where IWC exceeds 0.1 g m^{-3}. Such configuration leads to a lower rime mass fraction compared to the shallow system (Fig. 14).

5 Conclusions

This study aims to evaluate the implementation of predicted rime mass by means of a budget equation within DESCAM bin microphysics scheme by comparing the model outcomes to the ground based in situ and radar observations during the ICE-POP 2018 field campaign.

The new implementation within DESCAM consists in a binned distribution, tracking the rime mass of ice particles throughout their evolution as initially presented by Hashino and Tripoli (2007) as well as by Morrison and Grabowski (2008, 2010). The approach used here is based on the "fill-in" concept that considers the filling of the interstitial spaces of ice particles by rimed droplets, increasing the particle mass without changing its size. This allows for ice particles to have a smooth and free transition between unrimed and graupel particles. From the predicted rime mass, the terminal velocity (based on Heymsfield and Westbrook, 2010) and collision kernels were refined and set to be dependant on the rime fraction.

To assess the effect of these new implementations, DESCAM was applied to simulate a heavy snowfall event that was observed during the ICE-POP campaign over the Korean Peninsula between March 7-9, 2018. The model reproduced the two subsequent cloud systems observed during this event with, a deep system associated with a low pressure system, followed by a shallow orographic cloud field triggered by a moist marine easterly flow. Although the model missed the early part of the deep system, its intensity is similar to the observations in terms of radar reflectivity and precipitation rate. Furthermore, even if the shallow system intensity was occurring too early and its reflectivity was overestimated by +5 dB, both these discrepancies compensate the lack of precipitation accumulation due to the missed first part of the deep system. Another important bias of the model was also the formation of an upper cloud layer above 2 km altitude, likely caused by numerical humidity production at the outermost domain boundary conditions over mountainous regions, triggering ice nucleation processes.

The evolution of the simulated rime mass fraction at the MHS mountainous station successfully follows that of the riming index retrieved from the MASC instrument. This common evolution highlights the presence of rimed particles at the end of the deep system and during the shallow system. Our analysis indicates that riming events are associated with clouds generated by orographic lifting of easterly moist marine airflow, that promotes the presence of supercooled liquid water and favors riming.

The effect of the predicted rime implementation is especially visible for shallow cloud phase, where the number concentration of ice particles at ground doubles, leading to a close agreement with the observations. This implementation also leads to decrease the mean particle diameter from 1.5 mm to approximately 1 mm during the shallow phase, which is closer to the observed values around 0.5 mm diameter.

Regarding precipitation, the new DESCAM version causes an increase up to 10 mm in both ice and liquid precipitation over the mountainous southwestern regions of the Korean Peninsula. In total, the precipitation amount increases by 6.5%. Our results underscore the important role of ice particles representation for the production of ice and also liquid precipitation. However, the model still overestimates the ice particle size and underestimates the accumulated precipitation by around 5 mm compared to Pluvio measurements. Therefore, even if aggregation was refined in Grzegorczyk et al. (2025a), further improvements could be necessary, especially about the ice particle sticking efficiency which remains poorly documented.

Even if this study demonstrates that the rime properties of ice particles have a substantial effect and improve the simulated particle properties and precipitation amount of a snowfall event, it also motivates further new model developments. Additional predicted variables, such as rime volume (Morrison and Milbrandt, 2015), aspect ratio (Jensen and Harrington, 2015; Welss et al., 2024), or even water/ice ratio of ice particles (Planche et al., 2013a; Cholette et al., 2019), could be integrated into DESCAM to better represent the ice particle properties. Predicting rime volume would eliminate the need of a fixed m–D relation for graupel while a predicted aspect ratio could improve the representation of vapor deposition and enables more detailed comparisons with observations. The discussed and upcoming implementations could be confronted against different types of observations (e.g., in situ aircraft measurements) and applied to different kinds of case studies.

Appendix A: Transport of rime mass during vapor growth of ice particles

The variation of rime mass g_r for a bin of mass m_2 due to vapor deposition is calculated by:

$$\left(\frac{\partial g_r(m_2)}{\partial t}\right)_{dep} = \frac{1}{n_i(m_1)}\left(\frac{\partial n_i(m_1)}{\partial t}\right)_{dep} \times g_r(m_1) - \frac{1}{n_i(m_2)}\left(\frac{\partial n_i(m_2)}{\partial t}\right)_{dep} \times g_r(m_2) \tag{A1}$$

with $\left(\frac{\partial n_i(m_1)}{\partial t}\right)_{dep}$ the positive gain of ice particle number for the m_2 bin and $\left(\frac{\partial n_i(m_2)}{\partial t}\right)_{dep}$ the loss of ice particle number in the m_2 bin due to growth by vapor deposition. Both terms depend on the size of the particles, humidity as well as the advection scheme of Bott (1989) which calculates the change of particle number between the bins. These growth rates are normalized by the initial number of ice particles to obtain the fraction of ice particles that is transported. This proportion is then multiplied by the rime mass g_r to track the rime properties of the ice particles.

Appendix B: Radar dual wavelength ratio (DWR)

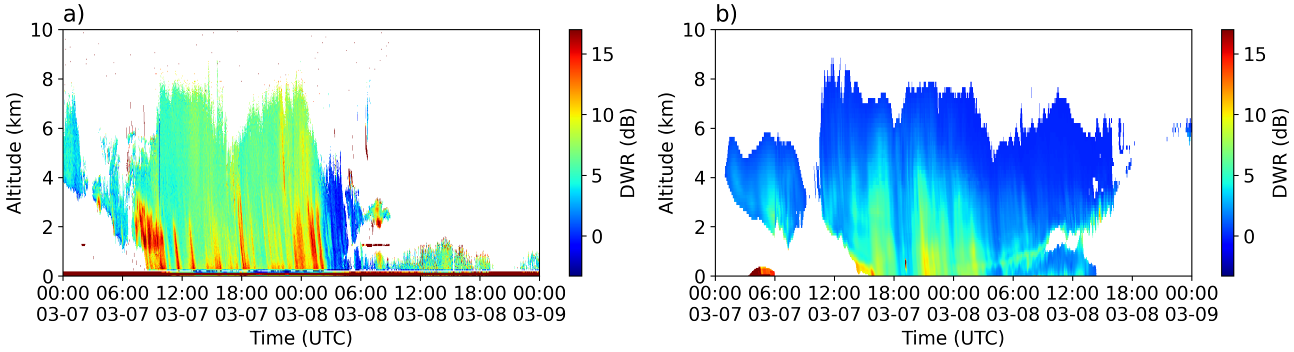

Figure A1. Radar dual wavelength ratio (DWR) between the X and W band (i.e. Z_X-Z_W) for a) radar observations and b) DESCAM control simulation. Only values corresponding to Z_X > -3 dBZ are shown.

Data availability. Details about the case study used in this work, provided for the 11th International Cloud Modeling Workshop (ICMW) 2024, are available here: https://iccp2024.kr/event/sub/6.%20Wintertime%20Orographic%20Precipitation%20Case%20from%20ICE-POP%202018.pdf. Parsivel, W-band radar, and MASC observations can be found via the PANGAEA repository: https://doi.org/10.1594/PANGAEA.918315 (Gehring et al., 2020a). Additional observational datasets provided for the 2024 ICMW are available here: https://zenodo.org/doi/10.5281/zenodo.17278661 (Grzegorczyk et al., 2025c). DESCAM-3D code is available upon request to celine.planche@uca.fr

Competing interests. The authors declare no competing interest.

Author contributions. PG: Draft the original manuscript, conducted the run and analysis of the numerical simulations, analyzed the observational datasets, and contributed to the conceptualization of the study. WW and AC: Edited the manuscript, performed numerical simulations, and conceptualized the study. FT: Edited the manuscript and analyzed the observational datasets. GL and KK: Edited the manuscript and processed the observational data. KSSL: Edited the manuscript and conceptualized the case study. CP: Edited the manuscript, conceptualized the study, supervised the project and acquired the funding.

Acknowledgements. The authors thank the participants of the World Weather Research Program Research Development Project and Forecast Demonstration Project, International Collaborative Experiments for PyeongChang 2018 Olympic and Paralympic winter games (ICE-POP 2018), hosted by the Korea Meteorological Administration. We also acknowledge the organizers and hosts of the 11th International Cloud

Modeling Workshop (ICMW) 2024, held at Yonsei University in Seoul, South Korea, in July 2024. We also thanks Jason Milbrandt for his contributions to the creation of the ICE-POP case study, as well as to all participants of the 2024 ICMW for their valuable input and constructive discussions about the case study. This work is part of project ACME funded by the Agence Nationale de la Recherche (ANR) under the JCJC program, reference ANR-21-CE01-0003. The contribution from the lead author has been founded by the ACME project. This work was granted access to the HPC resources of [CINES/IDRIS/TGCC] under the allocations A0100105056 and A0160115061 made by GENCI.

https://doi.org/10.5194/egusphere-2025-3202
Preprint. Discussion started: 14 October 2025

References

Abraham, F. F.: Functional Dependence of Drag Coefficient of a Sphere on Reynolds Number, Physics of Fluids, 13, 2194, https://doi.org/10.1063/1.1693218, 1970.

Arteaga, D., Planche, C., Kagkara, C., Wobrock, W., Banson, S., Tridon, F., and Flossmann, A.: Evaluation of Two Cloud-Resolving Models Using Bin or Bulk Microphysics Representation for the HyMeX-IOP7a Heavy Precipitation Event, Atmosphere, 11, 1177, https://doi.org/10.3390/atmos11111177, 2020.

Beard, K. V.: Terminal Velocity and Shape of Cloud and Precipitation Drops Aloft, Journal of the Atmospheric Sciences, 33, 851–864, https://doi.org/10.1175/1520-0469(1976)033<0851:tvasoc>2.0.co;2, 1976.

Bott, A.: A Positive Definite Advection Scheme Obtained by Nonlinear Renormalization of the Advective Fluxes, Monthly Weather Review, 117, 1006–1016, https://doi.org/10.1175/1520-0493(1989)117<1006:apdaso>2.0.co;2, 1989.

Bott, A.: A Flux Method for the Numerical Solution of the Stochastic Collection Equation, Journal of the Atmospheric Sciences, 55, 2284–2293, https://doi.org/10.1175/1520-0469(1998)055<2284:afmftn>2.0.co;2, 1998.

Böhm, H. P.: A General Equation for the Terminal Fall Speed of Solid Hydrometeors, Journal of Atmospheric Sciences, 46, 2419 – 2427, https://doi.org/10.1175/1520-0469(1989)046<2419:AGEFTT>2.0.CO;2, 1989.

Cholette, M., Morrison, H., Milbrandt, J. A., and Thériault, J. M.: Parameterization of the Bulk Liquid Fraction on Mixed-Phase Particles in the Predicted Particle Properties (P3) Scheme: Description and Idealized Simulations, Journal of the Atmospheric Sciences, 76, 561–582, https://doi.org/10.1175/jas-d-18-0278.1, 2019.

Clark, T., Hall, W., and Coen, J.: Source Code Documentation for the Clark-Hall Cloud-scale Model Code Version G3CH01, Tech. rep., https://doi.org/10.5065/D67W694V, 1996.

Clark, T. L.: Block-Iterative Method of Solving the Nonhydrostatic Pressure in Terrain-Following Coordinates: Two-Level Pressure and Truncation Error Analysis, Journal of Applied Meteorology, 42, 970–983, https://doi.org/10.1175/1520-0450(2003)042<0970:bmostn>2.0.co;2, 2003.

Cober, S. G. and List, R.: Measurements of the Heat and Mass Transfer Parameters Characterizing Conical Graupel Growth, Journal of the Atmospheric Sciences, 50, 1591–1609, https://doi.org/10.1175/1520-0469(1993)050<1591:motham>2.0.co;2, 1993.

Flossmann, A. I.: Interaction of Aerosol Particles and Clouds, Journal of the Atmospheric Sciences, 55, 879–887, https://doi.org/10.1175/1520-0469(1998)055<0879:ioapac>2.0.co;2, 1998.

Flossmann, A. I. and Wobrock, W.: A review of our understanding of the aerosol–cloud interaction from the perspective of a bin resolved cloud scale modelling, Atmospheric Research, 97, 478–497, https://doi.org/https://doi.org/10.1016/j.atmosres.2010.05.008, from the Lab to Models and Global Observations: Hans R. Pruppacher and Cloud Physics, 2010.

Flossmann, A. I. and Wobrock, W.: Cloud Processing of Aerosol Particles in Marine Stratocumulus Clouds, Atmosphere, 10, 520, https://doi.org/10.3390/atmos10090520, 2019.

Flossmann, A. I., Hall, W. D., and Pruppacher, H. R.: A Theoretical Study of the Wet Removal of Atmospheric Pollutants. Part I: The Redistribution of Aerosol Particles Captured through Nucleation and Impaction Scavenging by Growing Cloud Drops, Journal of the Atmospheric Sciences, 42, 583–606, https://doi.org/10.1175/1520-0469(1985)042<0583:atsotw>2.0.co;2, 1985.

Fontaine, E., Schwarzenboeck, A., Delanoë, J., Wobrock, W., Leroy, D., Dupuy, R., Gourbeyre, C., and Protat, A.: Constraining mass–diameter relations from hydrometeor images and cloud radar reflectivities in tropical continental and oceanic convective anvils, Atmospheric Chemistry and Physics, 14, 11 367–11 392, https://doi.org/10.5194/acp-14-11367-2014, 2014.

Garrett, T. J., Fallgatter, C., Shkurko, K., and Howlett, D.: Fall speed measurement and high-resolution multi-angle photography of hydrometeors in free fall, Atmospheric Measurement Techniques, 5, 2625–2633, https://doi.org/10.5194/amt-5-2625-2012, 2012.

Gehring, J., Ferrone, A., Billault-Roux, A.-C., Besic, N., and Berne, A.: Radar and ground-level measurements of precipitation during the ICE-POP 2018 campaign in South-Korea, https://doi.org/10.1594/PANGAEA.918315, 2020a.

Gehring, J., Oertel, A., Vignon, É., Jullien, N., Besic, N., and Berne, A.: Microphysics and dynamics of snowfall associated with a warm conveyor belt over Korea, Atmospheric Chemistry and Physics, 20, 7373–7392, https://doi.org/10.5194/acp-20-7373-2020, 2020b.

Gehring, J., Ferrone, A., Billault-Roux, A.-C., Besic, N., Ahn, K. D., Lee, G., and Berne, A.: Radar and ground-level measurements of precipitation collected by the École Polytechnique Fédérale de Lausanne during the International Collaborative Experiments for PyeongChang 2018 Olympic and Paralympic winter games, Earth System Science Data, 13, 417–433, https://doi.org/10.5194/essd-13-417-2021, 2021.

Geresdi, I.: Idealized simulation of the Colorado hailstorm case: comparison of bulk and detailed microphysics, Atmospheric Research, 45, 237–252, https://doi.org/10.1016/s0169-8095(97)00079-3, 1998.

Geresdi, I., Sarkadi, N., and Thompson, G.: Effect of the accretion by water drops on the melting of snowflakes, Atmospheric Research, 149, 96–110, https://doi.org/10.1016/j.atmosres.2014.06.001, 2014.

Grazioli, J., Lloyd, G., Panziera, L., Hoyle, C. R., Connolly, P. J., Henneberger, J., and Berne, A.: Polarimetric radar and in situ observations of riming and snowfall microphysics during CLACE 2014, Atmospheric Chemistry and Physics, 15, 13 787–13 802, https://doi.org/10.5194/acp-15-13787-2015, 2015.

Grzegorczyk, P., Yadav, S., Zanger, F., Theis, A., Mitra, S. K., Borrmann, S., and Szakáll, M.: Fragmentation of ice particles: laboratory experiments on graupel–graupel and graupel–snowflake collisions, Atmospheric Chemistry and Physics, 23, 13 505–13 521, https://doi.org/10.5194/acp-23-13505-2023, 2023.

Grzegorczyk, P., Wobrock, W., Canzi, A., Niquet, L., Tridon, F., and Planche, C.: Investigating secondary ice production in a deep convective cloud with a 3D bin microphysics model: Part I - Sensitivity study of microphysical processes representations, Atmospheric Research, 313, 107 774, https://doi.org/10.1016/j.atmosres.2024.107774, 2025a.

Grzegorczyk, P., Wobrock, W., Canzi, A., Niquet, L., Tridon, F., and Planche, C.: Investigating secondary ice production in a deep convective cloud with a 3D bin microphysics model: Part II - Effects on the cloud formation and development, Atmospheric Research, 314, 107 797, https://doi.org/10.1016/j.atmosres.2024.107797, 2025b.

Grzegorczyk, P., Wobrock, W., Canzi, A., Tridon, F., Lee, G., Kwonil, K., Lim, K.-S., and Planche, C.: Ground based observations of ICE-POP 2018 campaign used for DESCAM-3D, https://doi.org/10.5281/ZENODO.17278661, 2025c.

Hallett, J. and Mossop, S. C.: Production of secondary ice particles during the riming process, Nature, 249, 26–28, https://doi.org/10.1038/249026a0, 1974.

Hashino, T. and Tripoli, G. J.: The Spectral Ice Habit Prediction System (SHIPS). Part I: Model Description and Simulation of the Vapor Deposition Process, Journal of the Atmospheric Sciences, 64, 2210–2237, https://doi.org/10.1175/jas3963.1, 2007.

Hersbach, H., Bell, B., Berrisford, P., Hirahara, S., Horányi, A., Muñoz-Sabater, J., Nicolas, J., Peubey, C., Radu, R., Schepers, D., et al.: The ERA5 global reanalysis, Quarterly journal of the royal meteorological society, 146, 1999–2049, 2020.

Heymsfield, A., Szakáll, M., Jost, A., Giammanco, I., and Wright, R.: A Comprehensive Observational Study of Graupel and Hail Terminal Velocity, Mass Flux, and Kinetic Energy, Journal of the Atmospheric Sciences, 75, 3861–3885, https://doi.org/10.1175/jas-d-18-0035.1, 2018.

Heymsfield, A. J.: A Comparative Study of the Rates of Development of Potential Graupel and Hail Embryos in High Plains Storms, Journal of Atmospheric Sciences, 39, 2867 – 2897, https://doi.org/https://doi.org/10.1175/1520-0469(1982)039<2867:ACSOTR>2.0.CO;2, 1982.

Heymsfield, A. J. and Westbrook, C. D.: Advances in the Estimation of Ice Particle Fall Speeds Using Laboratory and Field Measurements, Journal of the Atmospheric Sciences, 67, 2469–2482, https://doi.org/10.1175/2010jas3379.1, 2010.

Heymsfield, A. J., Bansemer, A., Field, P. R., Durden, S. L., Stith, J. L., Dye, J. E., Hall, W., and Grainger, C. A.: Observations and Parameterizations of Particle Size Distributions in Deep Tropical Cirrus and Stratiform Precipitating Clouds: Results from In Situ Observations in TRMM Field Campaigns, Journal of the Atmospheric Sciences, 59, 3457–3491, https://doi.org/10.1175/1520-0469(2002)059<3457:oapops>2.0.co;2, 2002.

Hiron, T. and Flossmann, A. I.: A Study of the Role of the Parameterization of Heterogeneous Ice Nucleation for the Modeling of Microphysics and Precipitation of a Convective Cloud, Journal of the Atmospheric Sciences, 72, 3322–3339, https://doi.org/10.1175/jas-d-15-0026.1, 2015.

Hogan, R. J., Honeyager, R., Tyynelä, J., and Kneifel, S.: Calculating the millimetre-wave scattering phase function of snowflakes using the self-similar Rayleigh–Gans Approximation, Quarterly Journal of the Royal Meteorological Society, 143, 834–844, https://doi.org/10.1002/qj.2968, 2017.

Jensen, A. A. and Harrington, J. Y.: Modeling Ice Crystal Aspect Ratio Evolution during Riming: A Single-Particle Growth Model, Journal of the Atmospheric Sciences, 72, 2569–2590, https://doi.org/10.1175/jas-d-14-0297.1, 2015.

Jeoung, H., Liu, G., Kim, K., Lee, G., and Seo, E.-K.: Microphysical properties of three types of snow clouds: implication for satellite snowfall retrievals, Atmospheric Chemistry and Physics, 20, 14 491–14 507, https://doi.org/10.5194/acp-20-14491-2020, 2020.

Jin, H.-G., Lee, H., and Baik, J.-J.: A New Parameterization of the Accretion of Cloud Water by Graupel and Its Evaluation through Cloud and Precipitation Simulations, Journal of the Atmospheric Sciences, 76, 381–400, https://doi.org/10.1175/jas-d-18-0245.1, 2019.

Kagkara, C., Wobrock, W., Planche, C., and Flossmann, A. I.: The sensitivity of intense rainfall to aerosol particle loading – a comparison of bin-resolved microphysics modelling with observations of heavy precipitation from HyMeX IOP7a, Natural Hazards and Earth System Sciences, 20, 1469–1483, https://doi.org/10.5194/nhess-20-1469-2020, 2020.

Khain, A., Pokrovsky, A., Pinsky, M., Seifert, A., and Phillips, V.: Simulation of Effects of Atmospheric Aerosols on Deep Turbulent Convective Clouds Using a Spectral Microphysics Mixed-Phase Cumulus Cloud Model. Part I: Model Description and Possible Applications, Journal of the Atmospheric Sciences, 61, 2963–2982, https://doi.org/10.1175/jas-3350.1, 2004.

Khvorostyanov, V. I. and Curry, J. A.: Terminal Velocities of Droplets and Crystals: Power Laws with Continuous Parameters over the Size Spectrum, Journal of the Atmospheric Sciences, 59, 1872–1884, https://doi.org/10.1175/1520-0469(2002)059<1872:tvodac>2.0.co;2, 2002.

Khvorostyanov, V. I. and Curry, J. A.: Fall Velocities of Hydrometeors in the Atmosphere: Refinements to a Continuous Analytical Power Law, Journal of the Atmospheric Sciences, 62, 4343–4357, https://doi.org/10.1175/jas3622.1, 2005.

Kikuchi, K., Kameda, T., Higuchi, K., and Yamashita, A.: A global classification of snow crystals, ice crystals, and solid precipitation based on observations from middle latitudes to polar regions, Atmospheric Research, 132-133, 460–472, https://doi.org/10.1016/j.atmosres.2013.06.006, 2013.

Kim, K., Bang, W., Chang, E.-C., Tapiador, F. J., Tsai, C.-L., Jung, E., and Lee, G.: Impact of wind pattern and complex topography on snow microphysics during International Collaborative Experiment for PyeongChang 2018 Olympic and Paralympic winter games (ICE-POP 2018), Atmospheric Chemistry and Physics, 21, 11 955–11 978, https://doi.org/10.5194/acp-21-11955-2021, 2021.

King, W. D. and Fletcher, N. H.: Thermal Shock as an Ice Multiplication Mechanism. Part I. Theory, Journal of the Atmospheric Sciences, 33, 85–96, https://doi.org/10.1175/1520-0469(1976)033<0085:tsaaim>2.0.co;2, 1976.

Kneifel, S. and Moisseev, D.: Long-Term Statistics of Riming in Nonconvective Clouds Derived from Ground-Based Doppler Cloud Radar Observations, Journal of the Atmospheric Sciences, 77, 3495–3508, https://doi.org/10.1175/jas-d-20-0007.1, 2020.

Ko, J.-S., Lim, K.-S. S., Kim, K., Lee, G., Thompson, G., and Berne, A.: Simulated microphysical properties of winter storms from bulk-type microphysics schemes and their evaluation in the Weather Research and Forecasting (v4.1.3) model during the ICE-POP 2018 field campaign, Geoscientific Model Development, 15, 4529–4553, https://doi.org/10.5194/gmd-15-4529-2022, 2022.

Korolev, A. and Leisner, T.: Review of experimental studies of secondary ice production, Atmospheric Chemistry and Physics, 20, 11 767–11 797, https://doi.org/10.5194/acp-20-11767-2020, 2020.

Korolev, A., McFarquhar, G., Field, P. R., Franklin, C., Lawson, P., Wang, Z., Williams, E., Abel, S. J., Axisa, D., Borrmann, S., Crosier, J., Fugal, J., Krämer, M., Lohmann, U., Schlenczek, O., Schnaiter, M., and Wendisch, M.: Mixed-Phase Clouds: Progress and Challenges, Meteorological Monographs, 58, 5.1–5.50, https://doi.org/10.1175/amsmonographs-d-17-0001.1, 2017.

Kusunoki, K., Murakami, M., Orikasa, N., Hoshimoto, M., Tanaka, Y., Yamada, Y., Mizuno, H., Hamazu, K., and Watanabe, H.: Observations of Quasi-Stationary and Shallow Orographic Snow Clouds: Spatial Distributions of Supercooled Liquid Water and Snow Particles, Monthly Weather Review, 133, 743–751, https://doi.org/10.1175/mwr2874.1, 2005.

Kwon, J., Lim, K.-S. S., Park, S.-Y., Kim, K., and Lee, G.: Effects of Prognostic Number Concentrations of Snow and Graupel on the Simulated Precipitation over the Korean Peninsula, Weather and Forecasting, 38, 2591–2612, https://doi.org/10.1175/waf-d-23-0057.1, 2023.

Lee, J.-E., Jung, S.-H., Park, H.-M., Kwon, S., Lin, P.-L., and Lee, G.: Classification of precipitation types using fall velocity-diameter relationships from 2D-video distrometer measurements, Advances in Atmospheric Sciences, 32, 1277–1290, https://doi.org/10.1007/s00376-015-4234-4, 2015.

Leinonen, J., Kneifel, S., and Hogan, R. J.: Evaluation of the Rayleigh–Gans approximation for microwave scattering by rimed snowflakes, Quarterly Journal of the Royal Meteorological Society, 144, 77–88, https://doi.org/10.1002/qj.3093, 2017.

Leroy, D., Wobrock, W., and Flossmann, A. I.: On the influence of the treatment of aerosol particles in different bin microphysical models: A comparison between two different schemes, Atmospheric Research, 85, 269–287, https://doi.org/10.1016/j.atmosres.2007.01.003, 2007.

Leroy, D., Wobrock, W., and Flossmann, A. I.: The role of boundary layer aerosol particles for the development of deep convective clouds: A high-resolution 3D model with detailed (bin) microphysics applied to CRYSTAL-FACE, Atmospheric Research, 91, 62–78, https://doi.org/10.1016/j.atmosres.2008.06.001, 2009.

Lew, J. K., Kingsmill, D. E., and Montague, D. C.: A Theoretical Study of the Collision Efficiency of Small Planar Ice Crystals Colliding with Large Supercooled Water Drops, Journal of the Atmospheric Sciences, 42, 857–862, https://doi.org/10.1175/1520-0469(1985)042<0857:atsotc>2.0.co;2, 1985.

Li, J., Ye, Q., Li, F., and Chen, Y.: A cloud-resolving simulation study of monthly-scale autumn precipitation on Hainan Island: The effects of three categories of Graupel on rainfall, Atmospheric Research, 220, 92–108, https://doi.org/10.1016/j.atmosres.2019.01.008, 2019.

Lim, K.-S. S. and Hong, S.-Y.: Development of an Effective Double-Moment Cloud Microphysics Scheme with Prognostic Cloud Condensation Nuclei (CCN) for Weather and Climate Models, Monthly Weather Review, 138, 1587–1612, https://doi.org/10.1175/2009mwr2968.1, 2010.

Maherndl, N., Moser, M., Lucke, J., Mech, M., Risse, N., Schirmacher, I., and Maahn, M.: Quantifying riming from airborne data during the HALO-(AC)3campaign, Atmospheric Measurement Techniques, 17, 1475–1495, https://doi.org/10.5194/amt-17-1475-2024, 2024.

Mason, S. L., Chiu, C. J., Hogan, R. J., Moisseev, D., and Kneifel, S.: Retrievals of Riming and Snow Density From Vertically Pointing Doppler Radars, Journal of Geophysical Research: Atmospheres, 123, https://doi.org/10.1029/2018jd028603, 2018.

Matus, A. V. and L'Ecuyer, T. S.: The role of cloud phase in Earth's radiation budget, Journal of Geophysical Research: Atmospheres, 122, 2559–2578, https://doi.org/10.1002/2016jd025951, 2017.

McMillen, J. D. and Steenburgh, W. J.: Impact of Microphysics Parameterizations on Simulations of the 27 October 2010 Great Salt Lake–Effect Snowstorm, Weather and Forecasting, 30, 136–152, https://doi.org/10.1175/waf-d-14-00060.1, 2015.

Mitchell, D. L.: Use of Mass- and Area-Dimensional Power Laws for Determining Precipitation Particle Terminal Velocities, Journal of the Atmospheric Sciences, 53, 1710–1723, https://doi.org/10.1175/1520-0469(1996)053<1710:uomaad>2.0.co;2, 1996.

Mitchell, D. L. and Heymsfield, A. J.: Refinements in the Treatment of Ice Particle Terminal Velocities, Highlighting Aggregates, Journal of the Atmospheric Sciences, 62, 1637–1644, https://doi.org/10.1175/jas3413.1, 2005.

Mitchell, D. L., Zhang, R., and Pitter, R. L.: Mass-Dimensional Relationships for Ice Particles and the Influence of Riming on Snowfall Rates, Journal of Applied Meteorology, 29, 153–163, https://doi.org/10.1175/1520-0450(1990)029<0153:mdrfip>2.0.co;2, 1990.

Moisseev, D., von Lerber, A., and Tiira, J.: Quantifying the effect of riming on snowfall using ground-based observations, Journal of Geophysical Research: Atmospheres, 122, 4019–4037, https://doi.org/10.1002/2016jd026272, 2017.

Morrison, H. and Grabowski, W. W.: A Novel Approach for Representing Ice Microphysics in Models: Description and Tests Using a Kinematic Framework, Journal of the Atmospheric Sciences, 65, 1528–1548, https://doi.org/10.1175/2007jas2491.1, 2008.

Morrison, H. and Grabowski, W. W.: An Improved Representation of Rimed Snow and Conversion to Graupel in a Multicomponent Bin Microphysics Scheme, Journal of the Atmospheric Sciences, 67, 1337–1360, https://doi.org/10.1175/2010jas3250.1, 2010.

Morrison, H. and Milbrandt, J.: Comparison of Two-Moment Bulk Microphysics Schemes in Idealized Supercell Thunderstorm Simulations, Monthly Weather Review, 139, 1103–1130, https://doi.org/10.1175/2010mwr3433.1, 2011.

Morrison, H. and Milbrandt, J. A.: Parameterization of Cloud Microphysics Based on the Prediction of Bulk Ice Particle Properties. Part I: Scheme Description and Idealized Tests, Journal of the Atmospheric Sciences, 72, 287 – 311, https://doi.org/https://doi.org/10.1175/JAS-D-14-0065.1, 2015.

Morrison, H., Thompson, G., and Tatarskii, V.: Impact of Cloud Microphysics on the Development of Trailing Stratiform Precipitation in a Simulated Squall Line: Comparison of One- and Two-Moment Schemes, Monthly Weather Review, 137, 991–1007, https://doi.org/10.1175/2008mwr2556.1, 2009.

Newman, A. J., Kucera, P. A., and Bliven, L. F.: Presenting the Snowflake Video Imager (SVI), Journal of Atmospheric and Oceanic Technology, 26, 167–179, https://doi.org/10.1175/2008jtecha1148.1, 2009.

Park, J.-U., Kim, H.-J., Choi, J., Park, J.-S., Heo, J., and Kim, S.-W.: Observation of aerosol size distribution and new particle formation under different air masses arriving at the northwesternmost South Korean island in the Yellow Sea, Atmospheric Research, 255, 105 537, https://doi.org/10.1016/j.atmosres.2021.105537, 2021.

Park, S.-Y., Lim, K.-S. S., Kim, K., Lee, G., and Milbrandt, J. A.: Introducing graupel density prediction in Weather Research and Forecasting (WRF) double-moment 6-class (WDM6) microphysics and evaluation of the modified scheme during the ICE-POP field campaign, Geoscientific Model Development, 17, 7199–7218, https://doi.org/10.5194/gmd-17-7199-2024, 2024.

Pettersen, C., Bliven, L. F., von Lerber, A., Wood, N. B., Kulie, M. S., Mateling, M. E., Moisseev, D. N., Munchak, S. J., Petersen, W. A., and Wolff, D. B.: The Precipitation Imaging Package: Assessment of Microphysical and Bulk Characteristics of Snow, Atmosphere, 11, 785, https://doi.org/10.3390/atmos11080785, 2020.

Phillips, V. T. J., Patade, S., Gutierrez, J., and Bansemer, A.: Secondary Ice Production by Fragmentation of Freezing Drops: Formulation and Theory, Journal of the Atmospheric Sciences, 75, 3031–3070, https://doi.org/10.1175/jas-d-17-0190.1, 2018.

Pinty, J.-P. and Jabouille, P.: A mixed-phase cloud parameterization for use in mesoscale non-hydrostatic model: simulations of a squall line and of orographic precipitations, in: Conf. on cloud physics, pp. 217–220, Amer. Meteor. Soc. Everett, WA, 1998.

Planche, C., Wobrock, W., Flossmann, A. I., Tridon, F., Van Baelen, J., Pointin, Y., and Hagen, M.: The influence of aerosol particle number and hygroscopicity on the evolution of convective cloud systems and their precipitation: A numerical study based on the COPS observations on 12 August 2007, Atmospheric Research, 98, 40–56, https://doi.org/10.1016/j.atmosres.2010.05.003, 2010.

Planche, C., Wobrock, W., and Flossmann, A. I.: The continuous melting process in a cloud-scale model using a bin microphysics scheme: Continuous Melting Process in Bin Microphysics Scheme, Quarterly Journal of the Royal Meteorological Society, 140, 1986–1996, https://doi.org/10.1002/qj.2265, 2013a.

Planche, C., Wobrock, W., Flossmann, A. I., Tridon, F., Labbouz, L., and Van Baelen, J.: Small scale topography influence on the formation of three convective systems observed during COPS over the Vosges Mountains, Meteorologische Zeitschrift, 22, 395–411, https://doi.org/10.1127/0941-2948/2013/0402, 2013b.

Poirier, É., Thériault, J. M., and Leriche, M.: Role of sublimation and riming in the precipitation distribution in the Kananaskis Valley, Alberta, Canada, Hydrology and Earth System Sciences, 23, 4097–4111, https://doi.org/10.5194/hess-23-4097-2019, 2019.

Praz, C., Roulet, Y.-A., and Berne, A.: Solid hydrometeor classification and riming degree estimation from pictures collected with a Multi-Angle Snowflake Camera, Atmospheric Measurement Techniques, 10, 1335–1357, https://doi.org/10.5194/amt-10-1335-2017, 2017.

Seifert, A. and Beheng, K. D.: A two-moment cloud microphysics parameterization for mixed-phase clouds. Part 1: Model description, Meteorology and Atmospheric Physics, 92, 45–66, https://doi.org/10.1007/s00703-005-0112-4, 2006.

Seifert, A., Leinonen, J., Siewert, C., and Kneifel, S.: The Geometry of Rimed Aggregate Snowflakes: A Modeling Study, Journal of Advances in Modeling Earth Systems, 11, 712–731, https://doi.org/10.1029/2018ms001519, 2019.

Sunny Lim, K.-S., Chang, E.-C., Sun, R., Kim, K., Tapiador, F. J., and Lee, G.: Evaluation of Simulated Winter Precipitation Using WRF-ARW during the ICE-POP 2018 Field Campaign, Weather and Forecasting, 35, 2199–2213, https://doi.org/10.1175/waf-d-19-0236.1, 2020.

Takahashi, T., Nagao, Y., and Kushiyama, Y.: Possible High Ice Particle Production during Graupel–Graupel Collisions, Journal of the Atmospheric Sciences, 52, 4523–4527, https://doi.org/10.1175/1520-0469(1995)052<4523:phippd>2.0.co;2, 1995.

Thompson, G., Field, P. R., Rasmussen, R. M., and Hall, W. D.: Explicit Forecasts of Winter Precipitation Using an Improved Bulk Microphysics Scheme. Part II: Implementation of a New Snow Parameterization, Monthly Weather Review, 136, 5095–5115, https://doi.org/10.1175/2008mwr2387.1, 2008.

Tokay, A., Wolff, D. B., and Petersen, W. A.: Evaluation of the New Version of the Laser-Optical Disdrometer, OTT Parsivel2, Journal of Atmospheric and Oceanic Technology, 31, 1276–1288, https://doi.org/10.1175/jtech-d-13-00174.1, 2014.

Tridon, F., Battaglia, A., Chase, R. J., Turk, F. J., Leinonen, J., Kneifel, S., Mroz, K., Finlon, J., Bansemer, A., Tanelli, S., Heymsfield, A. J., and Nesbitt, S. W.: The Microphysics of Stratiform Precipitation During OLYMPEX: Compatibility Between Triple-Frequency Radar and Airborne In Situ Observations, Journal of Geophysical Research: Atmospheres, 124, 8764–8792, https://doi.org/10.1029/2018jd029858, 2019.

Tridon, F., Silber, I., Battaglia, A., Kneifel, S., Fridlind, A., Kalogeras, P., and Dhillon, R.: Highly supercooled riming and unusual triple-frequency radar signatures over McMurdo Station, Antarctica, Atmospheric Chemistry and Physics, 22, 12 467–12 491, https://doi.org/10.5194/acp-22-12467-2022, 2022.

Tsai, C., Kim, K., Liou, Y., Kim, J., Lee, Y., and Lee, G.: Orographic-Induced Strong Wind Associated With a Low-Pressure System Under Clear-Air Condition During ICE-POP 2018, Journal of Geophysical Research: Atmospheres, 127, https://doi.org/10.1029/2021jd036418, 2022.

Vié, B., Pinty, J.-P., Berthet, S., and Leriche, M.: LIMA (v1.0): A quasi two-moment microphysical scheme driven by a multimodal population of cloud condensation and ice freezing nuclei, Geoscientific Model Development, 9, 567–586, https://doi.org/10.5194/gmd-9-567-2016, 2016.

Vázquez-Martín, S., Kuhn, T., and Eliasson, S.: Shape dependence of snow crystal fall speed, Atmospheric Chemistry and Physics, 21, 7545–7565, https://doi.org/10.5194/acp-21-7545-2021, 2021.

Waitz, F., Schnaiter, M., Leisner, T., and Järvinen, E.: In situ observation of riming in mixed-phase clouds using the PHIPS probe, Atmospheric Chemistry and Physics, 22, 7087–7103, https://doi.org/10.5194/acp-22-7087-2022, 2022.

Wang, P. K. and Ji, W.: Collision Efficiencies of Ice Crystals at Low–Intermediate Reynolds Numbers Colliding with Supercooled Cloud Droplets: A Numerical Study, Journal of the Atmospheric Sciences, 57, 1001–1009, https://doi.org/10.1175/1520-0469(2000)057<1001:ceoica>2.0.co;2, 2000.

Welss, J., Siewert, C., and Seifert, A.: Explicit Habit-Prediction in the Lagrangian Super-Particle Ice Microphysics Model McSnow, Journal of Advances in Modeling Earth Systems, 16, https://doi.org/10.1029/2023ms003805, 2024.

Yadav, S., Metten, L., Grzegorczyk, P., Theis, A., Mitra, S. K., and Szakáll, M.: Measurement Report: Influence of particle density on secondary ice production by graupel and ice pellet collisions, EGUsphere, 2024, 1–15, https://doi.org/10.5194/egusphere-2024-3222, 2024.

Yum, S. S., Roberts, G., Kim, J. H., Song, K., and Kim, D.: Submicron aerosol size distributions and cloud condensation nuclei concentrations measured at Gosan, Korea, during the Atmospheric Brown Clouds–East Asian Regional Experiment 2005, Journal of Geophysical Research: Atmospheres, 112, https://doi.org/10.1029/2006jd008212, 2007.